Measurement of $e^+e^- \to \omega\pi^+\pi^-$ cross section at $\sqrt{s} = 2.000$ to 3.080 GeV

The BESIII collaboration

E-mail: besiii-publications@ihep.ac.cn

ABSTRACT: A partial wave analysis on the process $e^+e^- \to \omega\pi^+\pi^-$ is performed using $647\,\mathrm{pb}^{-1}$ of data sample collected by using the BESIII detector operating at the BEPCII storage ring at center-of-mass (c.m.) energies from $2.000\,\mathrm{GeV}$ to $3.080\,\mathrm{GeV}$. The Born cross section of the $e^+e^- \to \omega\pi^+\pi^-$ process is measured, with precision improved by a factor of 3 compared to that of previous studies. A structure near $2.25\,\mathrm{GeV}$ is observed in the energy-dependent cross sections of $e^+e^- \to \omega\pi^+\pi^-$ and $\omega\pi^0\pi^0$ with a statistical significance of 7.6σ, and its determined mass and width are $2232 \pm 19 \pm 27\,\mathrm{MeV}/c^2$ and $93 \pm 53 \pm 20\,\mathrm{MeV}$, respectively, where the first and second uncertainties are statistical and systematic, respectively. By analyzing the cross sections of subprocesses $e^+e^- \to \omega f_0(500)$, $\omega f_0(980)$, $\omega f_0(1370)$, $\omega f_2(1270)$, and $b_1(1235)\pi$, a structure, with mass $\mathrm{M} = 2200 \pm 11 \pm 17\,\mathrm{MeV}/c^2$ and width $\Gamma = 74 \pm 20 \pm 24\,\mathrm{MeV}$, is observed with a combined statistical significance of 7.9σ. The measured resonance parameters will help to reveal the nature of vector states around $2.25\,\mathrm{GeV}$.

Contents

1 Introduction

The experiment of electron-positron collisions has long been a research topic in elementary particle physics wherein searches for exotic hadronic states have continuously received much attention. Some exciting observations in the e^+e^- experiments have been recently reported in refs. [1–12]. Meanwhile, measurements of the cross sections of exclusive processes are of particular interest for resolving the discrepancy of muon magnetic anomaly $a_\mu = (g_\mu - 2)/2$ between experimental measurements and standard model (SM) predictions. The latest result by the Muon $g - 2$ Experiment shows 3.3 standard deviation from

the SM prediction [13], implying a hint for the existence of new physics [14]. However, to confirm this, further improvements in the precision for both experimental measurement and theoretical prediction are necessary. Specifically, the precision measurements on the cross sections of light hadron production in the e^+e^- annihilation are essential to reduce uncertainties of theoretical calculations on the hadronic vacuum polarization contribution and the muon anomaly a_μ [15–17].

The BaBar experiment has studied the process $e^+e^- \to \omega\pi^+\pi^-$ using the initial state radiation (ISR) method [18]. An indication of an isoscalar resonance structure near 2.25 GeV was observed in its Born cross section line shape [19]. The systems $\omega f_0(500)$, $\omega f_0(980)$, $\omega f_0(1370)$, and $\omega f_2(1270)$ have isospin zero, which are useful to search for excited ω and ϕ states, and important to confirm the structure near 2.25 GeV observed through the BaBar experiment [19]. This structure may correspond to $\phi(2170)$, $\omega(2205)$, $\omega(2290)$, and $\omega(2330)$, whose properties are poorly known in the particle data group (PDG) [20]. Many interpretations have been proposed for $\phi(2170)$, including a traditional $s\bar{s}$ state [21–26], an $s\bar{s}g$ hybrid [27, 28], an $ss\bar{s}\bar{d}$ tetraquark state [29–36], a $\Lambda\bar{\Lambda}$ bound state [37–41], and an ordinary resonant state of $\phi f_0(980)$ produced by the interactions between the final state particles [42, 43]. Recently, the $\phi(2170)$ state was examined through the BESIII experiment in the processes of $e^+e^- \to K^+K^-$ [44], $K^+K^-\pi^0\pi^0$ [45], $\phi\eta'$ [46], $\omega\eta$ [47], $K_S^0 K_L^0$ [48], $\phi\eta$ [49], and $2(K^+K^-)$, ϕK^+K^- [50]. The decay properties of $\omega(2205)$ as a candidate of $\omega(3D)$, $\omega(2290)$ and $\omega(2330)$ as candidates of $\omega(4S)$ states were discussed [51]. However, further experimental studies of the decay properties of these resonances are highly desired to reveal their natures.

In this paper, we report the measurement of Born cross sections for the $e^+e^- \to \omega\pi^+\pi^-$ process using the data collected in an energy scan at 19 c.m. energies ($\sqrt{s}$) from 2.000 GeV to 3.080 GeV with a total integrated luminosity of 647 pb^{-1}. The detailed values of c.m. energies and integrated luminosities of various data sets are presented in section 5.2. Combined with the previous measurements of the $e^+e^- \to \omega\pi^0\pi^0$ process [52], the cross sections of the $e^+e^- \to \omega\pi\pi$ process are obtained. In addition, the cross sections of the subprocesses via some intermediate states (e.g., $e^+e^- \to \omega f_0(500)$, $\omega f_0(980)$, $\omega f_0(1370)$, $\omega f_2(1270)$, and $b_1(1235)\pi$) are determined.

2 BESIII detector and Monte Carlo simulation

The BESIII detector [53] records symmetric e^+e^- collisions provided by the BEPCII storage ring [54], which operates in the c.m. energy range within 2.000–4.950 GeV. BESIII has collected large data samples in this energy region [55]. The cylindrical core of the BESIII detector covers 93% of the full solid angle and comprises a helium-based multilayer drift chamber (MDC), a plastic scintillator time-of-flight system (TOF), and a CsI(Tl) electromagnetic calorimeter (EMC), which are all enclosed in a superconducting solenoidal magnet providing a 1.0 T magnetic field. The solenoid is supported by an octagonal flux-return yoke with resistive plate counter muon identification modules interleaved with steel. The charged-particle momentum resolution at 1 GeV/c is 0.5%, and the specific ionization energy loss dE/dx resolution is 6% for electrons from Bhabha scattering. The EMC measures

photon energies with a resolution of 2.5% (5%) at 1 GeV in the barrel (end cap) region. The time resolution in the TOF barrel region is 68 ps, while that in the end cap region is 110 ps.

Monte-Carlo (MC) events, including the geometric description of the BESIII detector and the detector response, are produced using GEANT4-based [56] offline software BOSS [53]. Two million of inclusive MC events, $e^+e^- \to$ hadrons, are used to estimate the background contamination. They are generated using a hybrid generator, which integrates PHOKHARA [57, 58], ConExc [59, 60], and LUARLW [62] models. The PHOKHARA model generates 10 well parameterized and established exclusive channels. The ConExc model simulates a total of 47 exclusive processes according to a homogeneous and isotropic phase space population and then reproduces the measured line shapes of the absolute cross section. The remaining unknown decays of virtual photon are modeled by the LUARLW model.

Signal MC events for the $e^+e^- \to \omega\pi^+\pi^-$ process with subsequent decays $\omega \to \pi^+\pi^-\pi^0$ and $\pi^0 \to \gamma\gamma$ are generated by using the amplitude model with parameters fixed to the helicity amplitude analysis results, and the significant intermediate states are included with the ISR effects.

3 Event selection and background analysis

A data sample of the $e^+e^- \to \pi^+\pi^-\pi^+\pi^-\pi^0$ process is selected by requiring the net charge of four charged tracks to be zero and at least two photons. Charged tracks detected in the MDC are required to be within a polar angle (θ) range of $|\cos\theta|<0.93$, where θ is defined with respect to the z-axis, which is the symmetry axis of the MDC. For charged tracks, the distance of the closest approach to the interaction point (IP) must be less than 10 cm along the z-axis of the MDC, $|V_z|$, and less than 1 cm in the transverse plane, $|V_{xy}|$. Photon candidates are identified using showers in the EMC. The deposited energy of each shower is more than 25 MeV in the barrel region ($|\cos\theta|<0.80$) and more than 50 MeV in the end cap region ($0.86<|\cos\theta|<0.92$). To exclude showers that originate from charged tracks, the angle between the position of each shower in the EMC and the closest extrapolated charged track should be greater than 10 degrees. To suppress electronic noise and showers unrelated to the event, the difference between the EMC time and event start time must be within (0, 700) ns.

To improve the mass resolution and suppress the background contribution, a four-constraint (4C) kinematic fit imposing four-momentum conservation is performed under the hypothesis of the $e^+e^- \to 2(\pi^+\pi^-)\gamma\gamma$ process. When more than two photons exist, the combination with minimum χ^2_{4C} is retained for further analysis. Based on an optimization of the signal-to-noise ratio $\frac{N_s}{\sqrt{N_s+N_b}}$ for the requirement on χ^2_{4C}, where N_s and $N_s + N_b$ are the numbers of events in the ω signal region for signal MC sample and data, respectively, candidate events with $\chi^2_{4C} < 40$ are accepted for further analysis. The $\omega\pi^+\pi^-$ events are reconstructed by selecting the ω candidates from all the four $\pi^+\pi^-\pi^0$ combinations with minimal mass difference from the ω known mass [20]. The π^0 candidate is reconstructed by the $\gamma\gamma$ combination with a mass window of $0.12<M_{\gamma\gamma}<0.15 \,\text{GeV}/c^2$, and the ω signal region is defined with a requirement of $0.758<M_{\pi^+\pi^-\pi^0}<0.808 \,\text{GeV}/c^2$. To estimate the back-
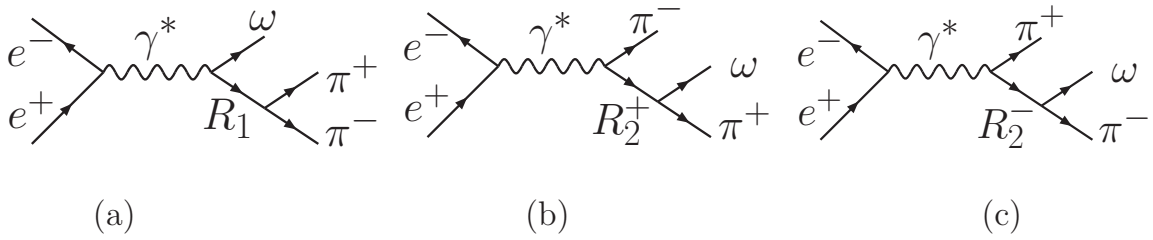
Figure 1. Feynman diagrams of the quasi-two body processes for $e^+e^- \to \omega\pi^+\pi^-$.

ground, the ω sidebands are defined as [0.733 , 0.758] GeV/c^2 and [0.808, 0.833] GeV/c^2. The $e^+e^- \to \pi^+\pi^-\pi^+\pi^-\pi^0$ process is found to be the dominant background source by analyzing the inclusive MC sample [63]. No peaking background is found in the signal region.

The selection of the 3π combination for ω candidate may lead to a wrong $\pi^+\pi^-\pi^0$ combination. The ratio due to the mis-combination is examined by matching the MC truth to the reconstructed final state particles using a sample of 0.5 million MC events for the $e^+e^- \to 2(\pi^+\pi^-)\pi^0$ process. When a charged pion is assigned to be from the wrong ω candidate, an event will be marked as "mis-combination". The ratio of the number of mis-combination ω to the total number of events is about 1.0% on average. The mis-combination yields will be subtracted from the ω candidate events when calculating the $e^+e^- \to \omega\pi^+\pi^-$ Born cross section.

4 Amplitude analysis

4.1 Kinematic variable

The $e^+e^- \to \omega\pi^+\pi^-$ events selected with the kinematic constraints are produced from the e^+e^- annihilation into a virtual photon, which then transformed to light quarks, followed by hadronization into the $\pi^+(p_1)\pi^-(p_2)\omega(p_3)$ final sates, where p_i ($i = 1, 2, 3$) denote the momenta reconstructed for the associated particles. The $e^+e^- \to \omega\pi^+\pi^-$ process may be from the quasi-two body process of $e^+e^- \to R_1\omega$, $R_1 \to \pi^+\pi^-$ (a); $e^+e^- \to \pi^-R_2^+$, $R_2^+ \to \pi^+\omega$ (b) and $e^+e^- \to \pi^+R_2^-$, $R_2^- \to \pi^-\omega$ (c), with Feynman diagrams shown in figure 1, where R_1 and $R_2^\pm$ denote the intermediate states. In the amplitude analysis, the intensity for each process is described with the helicity amplitude, which is constructed as the amplitude production of two sequential decays in the helicity frame. Taking process (a) as an example, figure 2 shows the definition of helicity rotation angles, where the R_1 polar angle, $\theta_{[12]}^{[123]}$, is defined as the angle spanned between the R_1 momentum and positron moving direction, and the azimuthal angle $\phi_{[12]}^{[123]}$ is the angle between the R_1 production plane and its decay plane. For the $R_1 \to \pi^+\pi^-$ decay, the azimuthal angle, $\phi_{[1]}^{[12]}$, is defined as the angle between the R_1 production plane and its decay plane, formed by the $\pi^+\pi^-$ momentum. After boosting the two pion momenta to the R_1 rest frame, they remain in the same decay plane. The polar angle $\theta_{[1]}^{[12]}$ for π^+ is defined as the angle between the $\pi^+\pi^-$ and R_1 momentum in the R_1 rest frame. Helicity angles for processes
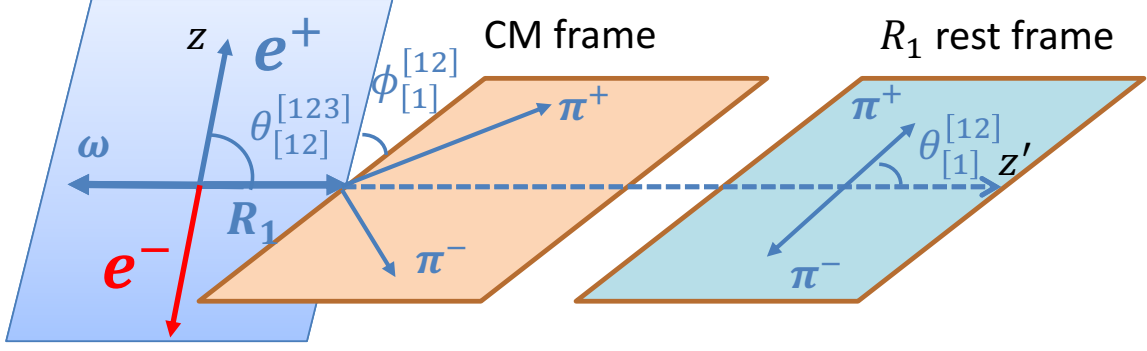
Figure 2. Helicity rotation angles defined for the process $e^+e^- \to R_1\omega, \ R_1 \to \pi^+\pi^-$.

Processes	Helicity angles	Amplitudes
$e^+e^- \to \gamma^*(m) \to R_1(\lambda_R)\omega(\lambda_3)$	$\theta^{[123]}_{[12]}, \phi^{[123]}_{[12]}$	$F^{\gamma^*}_{\lambda_R,\lambda_3}$
$R_1 \to \pi^+\pi^-$	$\theta^{[12]}_{[1]}, \phi^{[12]}_{[1]}$	$F^{R_1}_{0,0}$
$e^+e^- \to \gamma^*(m) \to R_2^+(\lambda_+)\pi^-$	$\theta^{[123]}_{[13]}, \phi^{[123]}_{[13]}$	$F^{\gamma^*}_{\lambda_+,0}$
$R_2^+ \to \omega(\lambda_3')\pi^+$	$\theta^{[13]}_{[3]}, \phi^{[13]}_{[3]}$	$F^{R_2^+}_{\lambda_3',0}$
$e^+e^- \to \gamma^*(m) \to R_2^-(\lambda_-)\pi^+$	$\theta^{[123]}_{[23]}, \phi^{[123]}_{[23]}$	$F^{\gamma^*}_{\lambda_-,0}$
$R_2^- \to \omega(\lambda_3'')\pi^-$	$\theta^{[23]}_{[3]}, \phi^{[23]}_{[3]}$	$F^{R_2^-}_{\lambda_3'',0}$

Table 1. Definitions of helicity angles and amplitudes for sequential processes (a), (b), and (c). Here, λ_i and m denote the helicity values for individual particle and the spin z projection of virtual photon in electron-positron annihilation.

(b) and (c) are defined in the same manner. Table 1 lists the definitions of helicity angles and amplitudes for the three processes.

4.2 Helicity amplitude

The amplitude for process (a) reads

$$A_1(m,\lambda_3) = \sum_{\lambda_R} F^{\gamma^*}_{\lambda_R,\lambda_3} D^{1*}_{m,\lambda_R-\lambda_3}(\phi^{[123]}_{[12]}, \theta^{[123]}_{[12]}, 0) BW(m_{12}) F^{R_1}_{0,0} D^{J*}_{\lambda_R,0}(\phi^{[12]}_{[1]}, \theta^{[12]}_{[1]}, 0), \quad (4.1)$$

where $D^J_{m,\lambda}(\phi,\theta,0)$ is the Wigner-D function, J is the spin of resonance R_1, and BW denotes the Breit-Wigner function.

The amplitude for process (b) reads

$$A_2(m,\lambda_3) = \sum_{\lambda_+,\lambda_3'} F^{\gamma^*}_{\lambda_+,0} D^{1*}_{m,\lambda_+}(\phi^{[123]}_{[13]}, \theta^{[123]}_{[13]}, 0) BW(m_{13}) F^{R_2^+}_{\lambda_3',0} D^{J*}_{\lambda_+,\lambda_3'}(\phi^{[13]}_{[3]}, \theta^{[13]}_{[3]}, 0)$$
$$\times D^1_{\lambda_3',\lambda_3}(\phi_3', \theta_3', 0), \quad (4.2)$$

where J is the spin of R_2^+. Since the ω helicity defined in this process is different from that defined in process (a), a rotation should be performed to align the ω helicity to

coincide with that in process (a) by the angle (θ_3', ϕ_3'). This issue has been addressed in the analyses [64, 65] and proved in ref. [66].

The amplitude for process (c) reads

$$
\begin{aligned}
A_3(m, \lambda_3) = \sum_{\lambda_-, \lambda_3''} & F_{\lambda_-,0}^{\gamma^*} D_{m,\lambda_-}^{1*}(\phi_{[23]}^{[123]}, \theta_{[23]}^{[123]}, 0) BW(m_{23}) F_{\lambda_3',0}^{R_2^-} D_{\lambda_-,\lambda_3''}^{J*}(\phi_{[3]}^{[23]}, \theta_{[3]}^{[23]}, 0) \\
& \times D_{\lambda_3'',\lambda_3}^{1}(\phi_3'', \theta_3'', 0),
\end{aligned}
\tag{4.3}
$$

where J is the spin of R_2^-. The Wigner function $D_{\lambda_3',\lambda_3}^{J}(\phi_3'', \theta_3'', 0)$ is used to align the ω helicity to coincide with that defined in process (a).

The non-resonant three-body process $e^+e^- \to \omega\pi^+\pi^-$ is also considered, and its amplitude is written as [67–70]:

$$
A_4(m, \lambda_3) = \sum_{\mu} F_{\mu,\lambda_3} D_{m,\mu}^{1*}(\alpha, \beta, \gamma),
\tag{4.4}
$$

where μ is the z-component of spin J in the helicity system; $m(\lambda_3)$ is the helicity value for $\gamma^*(\omega)$; α, β, γ are the Euler angles as defined in refs. [67–70]; and F_{μ,λ_3} is the helicity amplitude. The process conserves the parity and thus leads to $F_{\pm,\lambda_3} = -F_{\pm,-\lambda_3}$ and $F_{0,\lambda_3} = F_{0,-\lambda_3}$.

To match the covariant tensor amplitude, we expand the helicity amplitude in terms of the partial waves for the two-body process in the LS-coupling scheme [68–70]. It follows

$$
F_{\lambda,\nu}^{J} = \sum_{lS} \left(\frac{2l+1}{2J+1} \right)^{1/2} \langle l0S\delta | J\delta \rangle \langle s\lambda\sigma - \nu | S\delta \rangle g_{lS} r^l \frac{B_l(r)}{B_l(r_0)},
\tag{4.5}
$$

for a spin-J particle decay $J \to s + \sigma$, and λ and ν are the helicities of two final-state particles s and σ with $\delta = \lambda - \nu$. The symbol g_{lS} is a coupling constant, S is the total intrinsic spin $\mathbf{S} = \mathbf{s} + \sigma$, and l is the orbital angular momentum, $r = |\mathbf{r}|$, where $\mathbf{r}$ is the relative momentum between the two daughter particles in their mother rest frame and $\mathbf{r}_0$ corresponds to the invariant mass of the resonance which is equal to its nominal mass. The Blatt-Weisskopf factor $B_l(r)$ [68–70] up to $l = 4$ takes the form

$$
\begin{aligned}
B_0(r)/B_0(r_0) &= 1, \\
B_1(r)/B_1(r_0) &= \frac{\sqrt{1 + (dr_0)^2}}{\sqrt{1 + (dr)^2}}, \\
B_2(r)/B_2(r_0) &= \frac{\sqrt{9 + 3(dr_0)^2 + (dr_0)^4}}{\sqrt{9 + 3(dr)^2 + (dr)^4}}, \\
B_3(r)/B_3(r_0) &= \frac{\sqrt{225 + 45(dr_0)^2 + 6(dr_0)^4 + (dr_0)^6}}{\sqrt{225 + 45(dr)^2 + 6(dr)^4 + (dr)^6}}, \\
B_4(r)/B_4(r_0) &= \frac{\sqrt{11025 + 1575(dr_0)^2 + 135(dr_0)^4 + 10(dr_0)^6 + (dr_0)^8}}{\sqrt{11025 + 1575(dr)^2 + 135(dr)^4 + 10(dr)^6 + (dr)^8}},
\end{aligned}
\tag{4.6}
$$

where parameter d is constant fixed to $3\,\mathrm{GeV}^{-1}$ [64].

The differential cross section is given by

$$d\sigma = \frac{1}{2} \sum_{m,\lambda_3} \Omega(\lambda_3) \left| \sum_{i=1}^{3} A_i(m,\lambda_3) \right|^2 d\Phi, \tag{4.7}$$

where $m = \pm 1$ is due to the virtual photon produced from unpolarized e^+e^- annihilations, λ_3 is the ω helicity value, and $d\Phi$ is the element of a standard three-body phase space. The variable $\Omega(\lambda_3)(= |\varepsilon(\lambda_3) \cdot (\mathbf{q_1} \times \mathbf{q_2})|^2)$ is the ω decay matrix into the $\pi^+\pi^-\pi^0$ final states, where ε is the ω polarization vector and $\mathbf{q_1}(\mathbf{q_2})$ is the momentum vector for $\pi^+(\pi^-)$ from the ω decay. Here, we factor out the Breit-Wigner function describing the ω line shape into the MC integration when applying the amplitude model fit to the data events.

4.3 Simultaneous fit

The relative magnitudes and phases for coupling constants are determined by an unbinned maximum likelihood fit. The joint probability for observing N events in one data set is

$$\mathcal{L} = \prod_{i=1}^{N} P_i(p_1, p_2, p_3, p_4, p_5), \tag{4.8}$$

where p_j $(j = 1, 2, \ldots, 5)$ denote the four-vector momenta of the final states and P_i is a probability to produce event i with the momenta of the final states. The normalized P_i is calculated from the differential cross section

$$P_i = \frac{(d\sigma/d\Phi)_i}{\sigma_{\mathrm{MC}}}. \tag{4.9}$$

Here, the normalization factor σ_{MC} is calculated using a signal MC sample with N_{MC} accepted events, which are generated with a uniform distribution in phase space and subjected to the detector simulation, and then are passed through the same event selection criteria as applied to the data events. With a signal MC sample of two million events, the σ_{MC} is approximately evaluated as

$$\sigma_{\mathrm{MC}} \approx \frac{1}{N_{\mathrm{MC}}} \sum_{i=1}^{N_{\mathrm{MC}}} \left(\frac{d\sigma}{d\Phi} \right)_i. \tag{4.10}$$

For technical reasons, rather than maximizing $\mathcal{L}$, the object function, $S = -\ln\mathcal{L}$, is minimized using MINUIT [71]. To subtract the background events, the object function is replaced with

$$S = -\ln\mathcal{L} = -(\ln\mathcal{L}_{\mathrm{data}} - \ln\mathcal{L}_{\mathrm{bg}}), \tag{4.11}$$

where $\mathcal{L}_{\mathrm{data}}$ and $\mathcal{L}_{\mathrm{bg}}$ are the joint probability densities for data and background, respectively. The background events are obtained by the normalized ω sidebands.

We perform a simultaneous fit to an ensemble of the $\omega\pi^+\pi^-$ events with different c.m. energies, and their amplitudes sharing same coupling constants describing the intermediate state processes. The total object function is obtained as the summation of individual ones:

$$S' = -\sum_{j=1}^{N} \ln\mathcal{L}_j, \tag{4.12}$$

for the total N sets of data events.

After the parameters are determined in the fit, the signal yield of a given subprocess can be estimated by scaling its cross section ratio r_i to the number of net events

$$N_i = r_i(N_{\text{obs}} - N_{\text{bg}}), \text{ with } r_i = \frac{\sigma_i}{\sigma_{\text{tot}}}, \tag{4.13}$$

where σ_i is the cross section for the i-th subprocess as defined in eq. (4.7), σ_{tot} is the total cross section, N_{obs} is the number of observed events, and N_{bg} is the number of background events.

The statistical uncertainty, δN_i, associated with the signal yield N_i is estimated according to the error propagation formula using the covariance matrix V, obtained from the fit:

$$\delta N_i^2 = \sum_{m=1}^{N_{\text{pars}}} \sum_{n=1}^{N_{\text{pars}}} \left(\frac{\partial N_i}{\partial X_m} \frac{\partial N_i}{\partial X_n} \right)_{\mathbf{X}=\mu} V_{mn}(\mathbf{X}), \tag{4.14}$$

where $\mathbf{X}$ is a vector containing parameters and μ contains the fitted values for all parameters. The sum runs over all N_{pars} parameters.

4.4 Intermediate states and significance check

In terms of the $\pi^+\pi^-$ mass spectrum shown in figure 3 for 12 of the 19 samples, the $f_0(980)$ signals are significantly observed in the data events at c.m. energies below 2.3094 GeV. In the low $\pi^+\pi^-$ energy region, $f_0(500)$ resonance may have some contributions. In the high energy region, $f_0(1370)$ and $f_2(1270)$ resonances are included in the amplitude model. The $f_0(980)$ line shape is parameterized with the Flattê formula:

$$BW(s) = \frac{1}{s - m_0^2 + i(g_1\rho_{\pi\pi}(s) + g_2\rho_{K\bar{K}}(s))}, \tag{4.15}$$

where $\rho(s) = 2k/\sqrt{s}$; k is the c.m. momentum of the π or K in the resonance rest frame; g_1 and $\frac{g_2}{g_1}$ are fixed to the measured values of 0.138 ± 0.010 GeV^2 and 4.45 ± 0.25, respectively [72, 73]; and m_0 is the mass of the resonance $f_0(980)$ (m_0=0.990 GeV/c^2).

For the $f_0(500)$ line shape, many types of energy-dependence-width parameterizations exist in the literature [72, 73], among which we choose the E791 parameterizations (used by the E791 Collaboration) in the nominal fit:

$$BW(s) = \frac{1}{s - m_0^2 + i\sqrt{s}\Gamma}, \text{ with } \Gamma = \sqrt{1 - \frac{4m_\pi^2}{s}}\Gamma_0, \tag{4.16}$$

where m_0 and Γ_0 are the $f_0(500)$ mass and width, respectively.

For the other resonances (e.g., $f_0(1370)$, $f_2(1270)$, $b_1(1235)$, $\rho(1450)^\pm$ and $\rho(1570)^\pm$), the width is considered constant, and the line shape is described with the Breit-Weigner function, in which their masses and widths are fixed to the PDG values, as given in table 2.

The partial wave analysis (PWA) fit procedure begins by including all possible intermediate states in the PDG that match J^{PC} conservation in the subsequent two-body decay. Then we examine the statistical significance of the individual amplitudes. Amplitudes with statistical significance less then 5σ are dropped. This procedure is repeated until a baseline solution is obtained with only amplitudes having a statistical significance greater than 5σ.

Resonance	Mass (GeV/c^2)	Width (GeV)	Group A	Group B
$f_0(500)$	0.507 (0.400∼0.550)	0.475 (0.400∼0.700)	8.4σ	14.0σ
$f_0(980)$	0.990 ± 0.020	—	15.0σ	11.8σ
$f_0(1370)$	1.350 ± 0.050	0.200 ± 0.500	12.6σ	9.1σ
$f_2(1270)$	1.2755 ± 0.0008	0.1867 ± 0.0022	12.6σ	11.0σ
$b_1^{\pm}(1235)$	1.2295 ± 0.0032	0.142 ± 0.009	11.1σ	19.0σ
$\rho(1450)^{\pm}$	1.465 ± 0.025	0.400 ± 0.060	4.4σ	8.3σ
$\rho(1570)^{\pm}$	1.570 ± 0.070	0.144 ± 0.090	6.1σ	4.3σ

Table 2. Masses and widths of the intermediate states and statistical significances of individual intermediate processes in group A and group B data sets.

$\sqrt{s}$ (GeV)	$\omega f_0(500)$	$\omega f_0(980)$	$\omega f_0(1370)$	$\omega f_2(1270)$	$b_1^{\mp}(1235)\pi^{\pm}$	$\omega\pi^+\pi^-$
2.0000	58.6 ± 23.6	446.4 ± 42.4	200.4 ± 50.3	167.2 ± 26.8	27.8 ± 8.9	1.1 ± 1.1
2.1000	45.1 ± 19.9	578.4 ± 46.7	197.6 ± 46.3	130.0 ± 25.1	9.3 ± 6.6	10.9 ± 10.1
2.1250	720.2 ± 76.9	2281. ± 104.8	787.2 ± 117.8	759.5 ± 85.6	316.0 ± 41.1	24.6 ± 5.1
2.1750	130.3 ± 23.7	242.9 ± 29.7	59.0 ± 24.5	57.1 ± 20.3	55.4 ± 11.5	15.4 ± 8.1
2.2000	98.5 ± 20.7	262.9 ± 31.1	305.7 ± 47.0	146.7 ± 30.5	13.3 ± 7.8	13.0 ± 10.3
2.2324	100.5 ± 15.7	242.8 ± 25.7	187.7 ± 33.9	50.5 ± 14.6	23.9 ± 8.9	64.0 ± 8.8
2.3094	205.4 ± 41.7	63.0 ± 24.8	32.1 ± 26.9	145.8 ± 33.8	17.6 ± 9.9	12.1 ± 6.3
2.3864	115.1 ± 21.4	35.7 ± 15.4	72.7 ± 30.7	167.3 ± 32.5	26.2 ± 8.8	43.0 ± 7.3
2.3960	441.1 ± 42.3	70.8 ± 24.3	399.2 ± 62.4	115.6 ± 33.8	133.0 ± 27.5	15.4 ± 10.7
2.6444	97.6 ± 20.1	42.8 ± 14.8	49.2 ± 22.3	65.6 ± 19.8	42.9 ± 11.4	97.0 ± 22.2
2.6464	104.0 ± 15.6	85.6 ± 21.2	100.7 ± 25.8	69.2 ± 14.2	75.6 ± 10.3	18.3 ± 12.4
2.9000	194.0 ± 24.7	35.0 ± 17.2	47.4 ± 25.4	58.5 ± 19.1	112.0 ± 13.2	32.5 ± 6.7

Table 3. Signal yields of the subprocesses at various selected energy points, where the uncertainties are only statistical. The last column is the non-resonance part.

The 12 samples were divided into two groups, with group A including the energy points of $\sqrt{s} = 2.0000,\ 2.1000,\ 2.1250,\ 2.1750,\ 2.2000,\ 2.2324$ GeV, and group B including $\sqrt{s} = 2.3094,\ 2.3864,\ 2.3960,\ 2.6444,\ 2.6464,\ 2.9000$ GeV according to the $\pi^+\pi^-$ invariant mass distributions at various energy points.

The statistical significance of each amplitude is evaluated by incorporating the changes in likelihood and number of degrees of freedom with and without the corresponding amplitude being included in the simultaneous fit. The significance for each intermediate state is listed in table 2. We take the subprocess with a significance greater than 5σ in both group A and group B data sets to be the baseline solutions, including the $e^+e^- \to \omega f_0(500),\ \omega f_0(980),\ \omega f_0(1370),\ \omega f_2(1270)$ and $b_1^{\mp}(1235)\pi^{\pm}$ processes.

4.5 Fit results

Signal yields for the data sets are calculated using eq. (4.13), and their statistical uncertainties are derived using eq. (4.14), which includes the correlation among parameters. The signal yields are given in table 3. Projections of invariant masses for individual energy points are shown in figure 3. The combined energy points of mass projections of fit results for groups A and B are shown in figure 4 and figure 5, respectively.

5 Born cross section

5.1 ISR correction factor

In the direct e^+e^- collision experiments, the observed cross section, $\sigma_{\text{obs}}(s)$, at the c.m. energy $\sqrt{s}$ for $e^+e^- \to \omega\pi^+\pi^-$ is the Born cross section, $\sigma_0(s)$, convolved with the ISR function $W(s, x)$ [60, 61]. To unfold the Born cross section, the ISR correction factor should be defined as

$$1 + \delta = \frac{\sigma_{\text{obs}}(s)}{\sigma_0(s)}, \tag{5.1}$$

with

$$\sigma_{\text{obs}}(s) = \int_{M_{\text{th}}}^{\sqrt{s}} W(s, x) \frac{\sigma_0[s(1-x)]}{|1 - \Pi(\sqrt{s})|^2} dx, \tag{5.2}$$

where $\Pi(\sqrt{s})$ is the vacuum polarization function. We use the calculated results, including the leptonic and hadronic parts both in space- and time-like regions [74–78]. The M_{th} corresponds to the $\omega\pi^+\pi^-$ mass threshold, and x is the ratio of the ISR photon energy to the beam energy.

Calculations of the ISR correction factor and the MC event generation are consistently performed using the generator model "ConExc" [60], and the dressed cross sections $\sigma_0^D(s)$ are taken from the BaBar experiment ($\sqrt{s} < 2.000\,\text{GeV}$) [18] and this measurement ($\sqrt{s} > 2.000\,\text{GeV}$). To achieve stable cross sections in this measurement, the procedure of the ISR correction factor calculation and the MC event generation for the Born cross section calculation are iterated serval times. The iteration is stopped if the updated Born cross section reaches the accuracy within statistical uncertainty. The ISR correction factors for various energy points are given in table 4.

In the MC event generation, the ISR photon is characterized by the soft energy and beam collinear distribution. Its angular dependence is sampled with the Bonneau and Martin formula with an accuracy of up to the m_e^2/s term;

$$P(\theta, x) = \frac{\sin^2\theta - \frac{x^2\sin^4\theta}{2(x^2-2x+2)} - \frac{m_e^2}{E^2}\frac{(1-2x)\sin^2\theta - x^2\cos^4\theta}{x^2-2x+2}}{\left(\sin^2\theta + \frac{m_e^2}{E^2}\cos^2\theta\right)^2}, \tag{5.3}$$

where θ is the polar angle of the ISR photon, m_e is the electron mass, and E is the beam energy. After the photon emission, the $\gamma^* \to \omega\pi^+\pi^-$ events are generated with the amplitude model with parameters fixed to the fitted values so that the measured intermediate states are inclusively simulated. Figure 6 shows an example of the MC simulation at $\sqrt{s} = 2.125\,\text{GeV}$, in which we can observe a good agreement between data and MC simulation in the mass distribution.
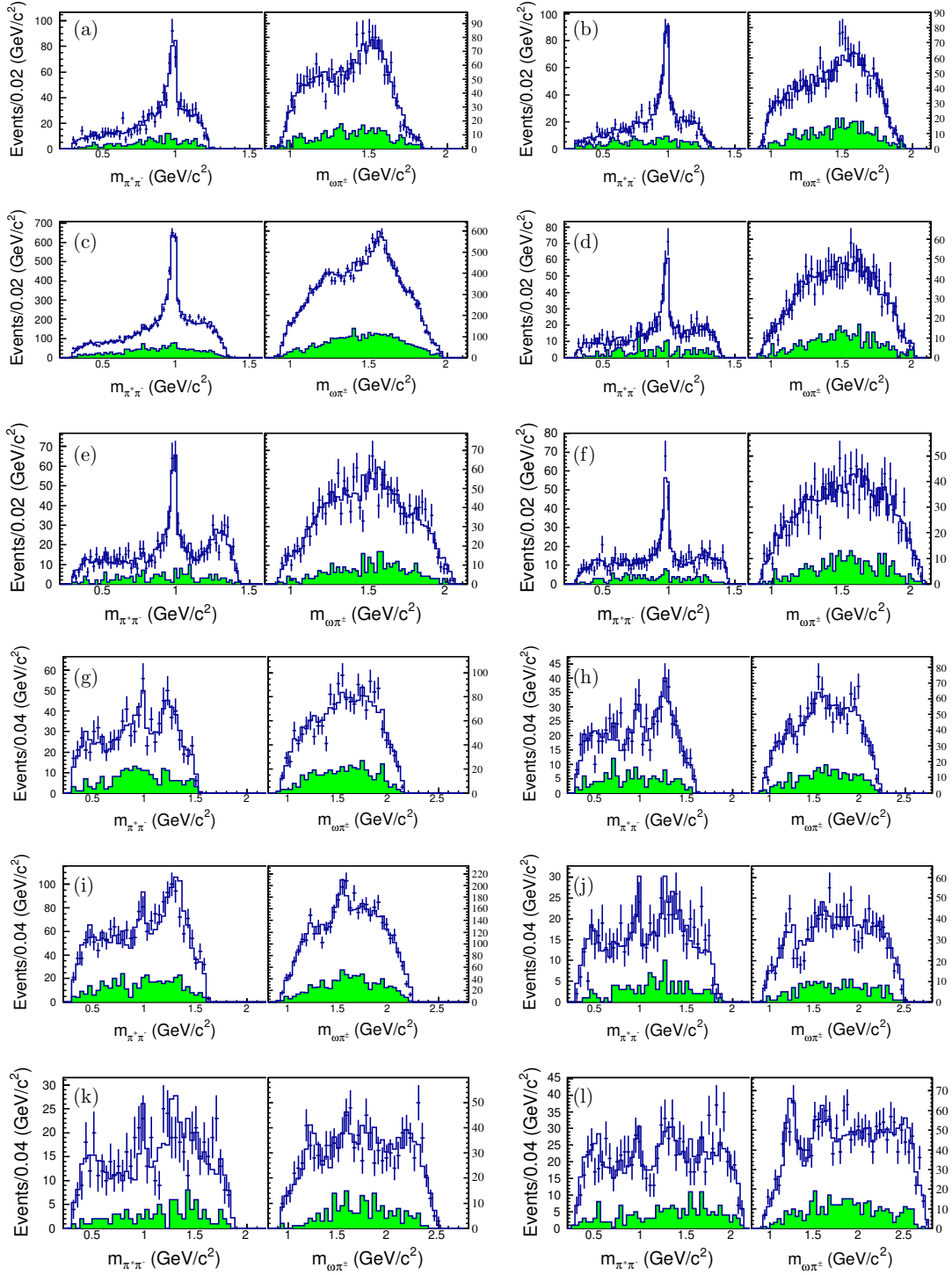
Figure 3. Projections of the fit results for mass spectra $m_{\pi^+\pi^-}$ and $m_{\omega\pi^\pm}$ for selected energy points. Dots with error bars are the data, histograms are the projection of the fit results, and shaded histograms (green) are the background estimated by the ω mass sideband. The subplots are for data sets $\sqrt{s} = $ 2.0000 (a), 2.1000 (b), 2.1250 (c), 2.1750 (d), 2.2000 (e), 2.2324 (f), 2.3094 (g), 2.3864 (h), 2.3960 (i), 2.6444 (j), 2.6464 (k), and 2.9000 (l) GeV.
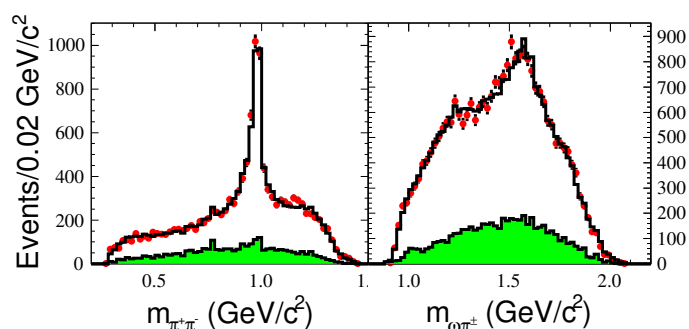
Figure 4. Projections of the fit results for mass spectra $m_{\pi^+\pi^-}$ and $m_{\omega\pi^\pm}$ for group A data sets. Dots with error bars are the data, histograms are the projection of the total fit results, and shaded histograms (green) are the background estimated by the ω mass sideband.
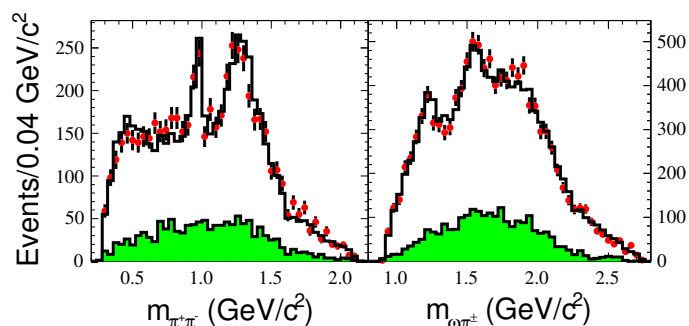

Figure 5. Projections of the fit results for mass spectra $m_{\pi^+\pi^-}$ and $m_{\omega\pi^\pm}$ for group B data sets. Dots with error bars are the data, histograms are the total fit results, and shaded histograms (green) are the background estimated by the ω mass sideband.
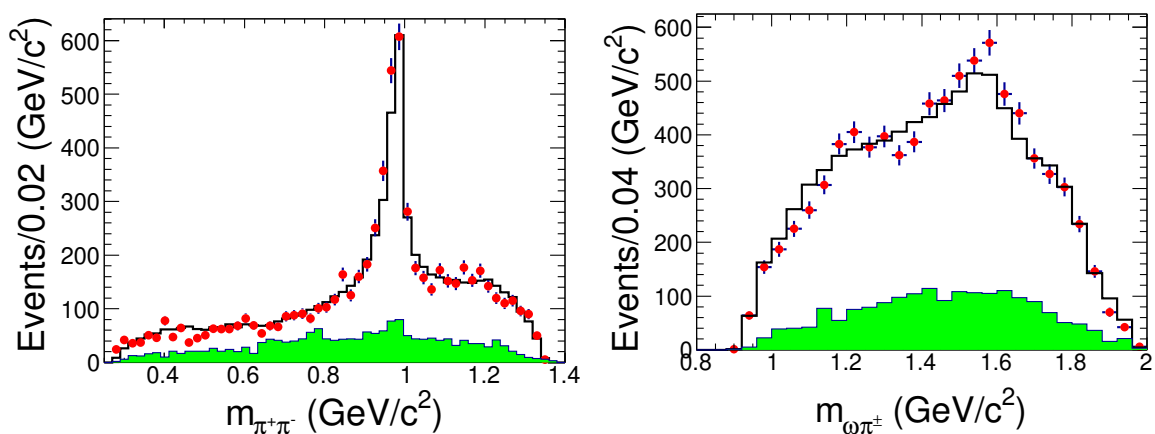

Figure 6. Comparison of $m_{\pi^+\pi^-}$ and $m_{\omega\pi^\pm}$ mass spectra between data and MC simulation at $\sqrt{s} = 2.1250\,\text{GeV}$. Dots with error bars are the data, histograms are the MC simulation, and shaded histograms (green) are the background estimated by the ω mass sideband.
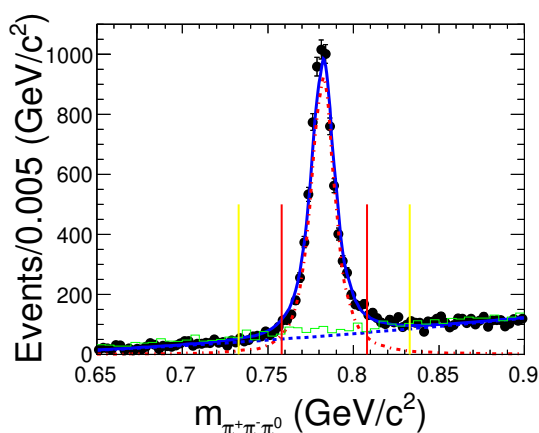
Figure 7. The $\pi^+\pi^-\pi^0$ invariant mass spectrum of the process $e^+e^- \to \omega\pi^+\pi^-$ at $\sqrt{s} = 2.1250\,\text{GeV}$. The dots with error bars are the data, the red dotted curve is the signal, and the blue dashed line is the background. The blue solid curve is the best fit result. The green histogram is from the MC simulation of the non-resonant contribution from $e^+e^- \to \pi^+\pi^-\pi^+\pi^-\pi^0$. The range between the two red vertical solid lines is regarded as the signal region, and those between the yellow and red vertical lines on each side of the signal peak are regarded as the sideband regions.

5.2 Cross section for $e^+e^- \to \omega\pi^+\pi^-$

The signal yields are determined by an unbinned maximum likelihood fit to the $\pi^+\pi^-\pi^0$ invariant mass distribution of the ω candidates. In the fit, the signal shape is modeled with the MC histogram smeared with a Gaussian function for the resolution difference between data and MC simulation. The background is dominated by the process $e^+e^- \to 2(\pi^+\pi^-)\pi^0$, and the corresponding shape is described by a second-order Chebychev polynomial. The parameters of the Gaussian function, the background polynomial and the yields of signal and background are floated. Figure 7 shows the fit results at $\sqrt{s} = 2.125\,\text{GeV}$. The Born cross section is calculated from

$$\sigma^B = \frac{N_{\text{sig}} - N_{\text{mis}}}{\mathcal{L} \cdot \epsilon \cdot Br(\omega \to \pi^+\pi^-\pi^0) \cdot Br(\pi^0 \to \gamma\gamma) \cdot (1+\delta)}, \tag{5.4}$$

where N_{sig} is the number of signal events obtained by fitting the $\pi^+\pi^-\pi^0$ mass distribution, N_{mis} the mis-combination yield, $\mathcal{L}$ the integrated luminosity, and ϵ the detection efficiency obtained from the MC simulation according to the PWA result. $Br(\omega \to \pi^+\pi^-\pi^0)$ and $Br(\pi^0 \to \gamma\gamma)$ are the branching fractions quoted from the PDG [20], and $(1+\delta)$ represents the correction factors due to the ISR effect and vacuum polarization. The resulting Born cross sections and related variables are summarized in table 4.

5.3 Cross sections for the intermediate subprocesses

The Born cross sections for the intermediate subprocesses are determined with the total Born cross sections of the $e^+e^- \to \omega\pi^+\pi^-$ process and the PWA results. Using a signal MC sample of events generated uniformly in the phase space without the ISR effect, the

$\sqrt{s}$ (GeV)	N_{sig}	N_{mis}	$\mathcal{L}(\text{pb}^{-1})$	$1 + \delta$	ϵ	σ^B(pb)
2.0000	1008 $\pm$ 37	10 $\pm$ 3	10.1	1.1819	0.1775	534.3 $\pm$ 19.8 $\pm$ 29.9
2.0500	239 $\pm$ 18	3 $\pm$ 2	3.4	1.1912	0.1615	421.3 $\pm$ 32.0 $\pm$ 23.4
2.1000	952 $\pm$ 37	9 $\pm$ 3	12.2	1.1707	0.1764	424.6 $\pm$ 16.7 $\pm$ 22.7
2.1250	8013 $\pm$ 103	80 $\pm$ 9	109.0	1.1715	0.1704	413.6 $\pm$ 5.4 $\pm$ 22.3
2.1500	207 $\pm$ 17	2 $\pm$ 1	2.9	1.1649	0.1587	446.4 $\pm$ 37.4 $\pm$ 29.1
2.1750	863 $\pm$ 34	9 $\pm$ 3	10.6	1.1789	0.1646	471.0 $\pm$ 18.8 $\pm$ 24.6
2.2000	971 $\pm$ 36	10 $\pm$ 3	13.7	1.1858	0.1631	411.5 $\pm$ 15.4 $\pm$ 21.4
2.2324	821 $\pm$ 32	8 $\pm$ 3	11.9	1.1986	0.1556	415.6 $\pm$ 16.4 $\pm$ 23.0
2.3094	856 $\pm$ 35	9 $\pm$ 3	21.1	1.2543	0.1503	241.6 $\pm$ 10.0 $\pm$ 14.4
2.3864	664 $\pm$ 30	7 $\pm$ 3	22.6	1.3953	0.1470	160.8 $\pm$ 7.3 $\pm$ 8.4
2.3960	1943 $\pm$ 53	19 $\pm$ 4	66.9	1.4114	0.1324	174.9 $\pm$ 4.8 $\pm$ 9.5
2.6444	624 $\pm$ 29	6 $\pm$ 2	33.7	1.4456	0.1228	117.2 $\pm$ 5.5 $\pm$ 6.3
2.6464	606 $\pm$ 29	6 $\pm$ 2	34.1	1.4463	0.1481	93.2 $\pm$ 4.5 $\pm$ 5.3
2.9000	999 $\pm$ 36	10 $\pm$ 3	106.0	1.6241	0.1035	63.0 $\pm$ 2.3 $\pm$ 3.6
2.9500	136 $\pm$ 14	2 $\pm$ 1	16.0	1.5524	0.1044	59.9 $\pm$ 5.9 $\pm$ 3.9
2.9810	130 $\pm$ 13	2 $\pm$ 1	16.1	1.5029	0.1101	55.3 $\pm$ 5.6 $\pm$ 3.3
3.0000	119 $\pm$ 12	1 $\pm$ 1	15.9	1.5038	0.1076	52.7 $\pm$ 5.4 $\pm$ 3.5
3.0200	134 $\pm$ 13	2 $\pm$ 1	17.3	1.5308	0.1058	54.1 $\pm$ 5.3 $\pm$ 3.2
3.0800	543 $\pm$ 28	5 $\pm$ 3	126.2	1.7893	0.0776	35.2 $\pm$ 1.8 $\pm$ 2.6

Table 4. Summary of the signal yield (N_{sig}), number of mis-combination events (N_{mis}), integrated luminosity $\mathcal{L}$, ISR correction factor ($1 + \delta$), detection efficiency (ϵ), and total Born cross section of $e^+e^- \to \omega\pi^+\pi^-$ (σ^B) at various energy points $\sqrt{s}$. The uncertainties of N_{sig} and N_{mis} are only statistical. The first and second uncertainties of Born cross sections are statistical and systematic, respectively.

ratio of the Born cross section for a subprocess R to the total cross section is determined.

$$r_R = \frac{\sigma_R}{\sigma_{\text{tot}}}, \tag{5.5}$$

where σ_R and σ_{tot} are obtained by the partial wave amplitude weighted MC sample. The Born cross sections of the intermediate subprocess at each of the selected energy points are given in table 5.

6 Systematic uncertainties

6.1 Uncertainties for intermediate subprocesses

The uncertainties for the measurements of intermediate subprocesses due to the PWA originate from the parameterizations of the $f_0(500)$ and $f_0(980)$ states, the resonance parameters, insignificant contributions for some intermediate states, and background contamination.

$\sqrt{s}$ (GeV)	$\omega f_0(500)$	$\omega f_0(980)$	$\omega f_0(1370)$
2.0000	$37.7 \pm 15.2 \pm 5.0$	$237.3 \pm 22.6 \pm 31.3$	$114.0 \pm 28.6 \pm 15.1$
2.1000	$34.7 \pm 15.3 \pm 5.5$	$117.1 \pm\ \ 9.5 \pm 18.6$	$60.3 \pm 14.1 \pm\ \ 9.6$
2.1250	$45.6 \pm\ \ 4.9 \pm 5.0$	$144.3 \pm\ \ 6.6 \pm 15.7$	$49.8 \pm\ \ 7.5 \pm\ \ 5.4$
2.1750	$91.1 \pm 16.6 \pm 6.7$	$210.1 \pm 25.7 \pm 38.5$	$90.3 \pm 37.5 \pm 16.5$
2.2000	$78.2 \pm 16.4 \pm 7.0$	$133.4 \pm 15.8 \pm 29.0$	$155.1 \pm 23.9 \pm 33.7$
2.2324	$63.8 \pm 10.0 \pm 2.5$	$154.1 \pm 16.3 \pm 30.1$	$119.2 \pm 21.5 \pm 23.3$
2.3094	$73.1 \pm 14.9 \pm 3.0$	$52.4 \pm 20.6 \pm\ \ 9.3$	$42.4 \pm 35.5 \pm\ \ 7.5$
2.3864	$34.5 \pm\ \ 6.4 \pm 5.8$	$30.7 \pm 13.2 \pm\ \ 5.2$	$21.8 \pm\ \ 9.2 \pm\ \ 3.7$
2.3960	$50.4 \pm\ \ 4.8 \pm 1.5$	$48.1 \pm 16.5 \pm 11.0$	$45.6 \pm\ \ 7.1 \pm 10.5$
2.6444	$23.1 \pm\ \ 4.8 \pm 2.2$	$10.1 \pm\ \ 3.5 \pm\ \ 1.0$	$11.6 \pm\ \ 5.3 \pm\ \ 1.1$
2.6464	$20.3 \pm\ \ 3.1 \pm 3.8$	$16.7 \pm\ \ 4.2 \pm\ \ 3.2$	$19.6 \pm\ \ 5.0 \pm\ \ 3.7$
2.9000	$15.7 \pm\ \ 2.0 \pm 1.7$	$2.8 \pm\ \ 1.4 \pm\ \ 0.3$	$3.8 \pm\ \ 2.0 \pm\ \ 0.4$

$\sqrt{s}$ (GeV)	$\omega f_2(1270)$	$b_1^{\pm}(1235)\pi^{\mp}$	non-resonant $\omega\pi^+\pi^-$
2.0000	$107.6 \pm 17.3 \pm 14.2$	$17.9 \pm\ \ 5.7 \pm 2.4$	$1.9 \pm\ \ 1.9 \pm 0.1$
2.1000	$71.3 \pm 13.8 \pm 11.3$	$10.2 \pm\ \ 7.3 \pm 1.6$	$6.0 \pm\ \ 5.6 \pm 0.3$
2.1250	$48.0 \pm\ \ 5.4 \pm\ \ 5.3$	$19.9 \pm\ \ 2.6 \pm 2.2$	$1.6 \pm\ \ 0.3 \pm 0.1$
2.1750	$56.1 \pm 19.9 \pm 10.3$	$39.1 \pm\ \ 8.1 \pm 7.2$	$3.6 \pm\ \ 1.9 \pm 0.2$
2.2000	$90.3 \pm 18.8 \pm 19.6$	$26.8 \pm 15.7 \pm 5.8$	$6.1 \pm\ \ 4.8 \pm 0.3$
2.2324	$49.2 \pm 14.2 \pm\ \ 9.6$	$15.2 \pm\ \ 5.7 \pm 3.0$	$8.3 \pm\ \ 1.2 \pm 0.5$
2.3094	$43.4 \pm 10.1 \pm\ \ 7.7$	$6.3 \pm\ \ 3.6 \pm 1.1$	$0.8 \pm\ \ 0.4 \pm 0.1$
2.3864	$22.4 \pm\ \ 4.4 \pm\ \ 3.8$	$7.9 \pm\ \ 2.7 \pm 1.3$	$9.6 \pm\ \ 1.6 \pm 0.5$
2.3960	$13.2 \pm\ \ 3.9 \pm\ \ 3.0$	$15.2 \pm\ \ 3.1 \pm 3.5$	$0.7 \pm\ \ 0.5 \pm 0.1$
2.6444	$15.5 \pm\ \ 4.7 \pm\ \ 1.5$	$10.2 \pm\ \ 2.7 \pm 1.0$	$2.4 \pm\ \ 0.5 \pm 0.1$
2.6464	$13.5 \pm\ \ 2.8 \pm\ \ 2.6$	$14.8 \pm\ \ 2.0 \pm 2.8$	$1.9 \pm\ \ 1.3 \pm 0.1$
2.9000	$4.7 \pm\ \ 1.6 \pm\ \ 0.5$	$9.0 \pm\ \ 1.1 \pm 1.0$	$2.9 \pm\ \ 0.6 \pm 0.2$

Table 5. Born cross sections for the subprocesses at various selected energy points in unit of pb, where the first and second uncertainties are statistical and systematic, respectively.

- In the nominal fit, we take the $f_0(500)$ line shape as that used by the E791 Collaboration. The uncertainty associated with this parametrization is estimated by replacing it with those in ref. [73]. The difference in the signal yield of each intermediate state is considered as the systematic uncertainty.

- The parameters of the $f_0(980)$ Flattê formula in the nominal fit are fixed to the measurements [72, 73]. The uncertainties are estimated by varying the resonance parameters by one standard deviation. The differences in the signal yields are considered as the systematic uncertainties.

- The masses and widths of intermediate states $f_0(1370)$, $f_2(1270)$, and $b_1(1235)$ are fixed to the PDG values [20] in the nominal fit. The associated uncertainties are estimated by varying masses and widths by $\pm 1\sigma$ respectively. The differences are taken as the corresponding systematic uncertainties.

- The two resonances $\rho(1450)^{\pm}$ and $\rho(1570)^{\pm}$ are insignificant and not included in the baseline solution. The differences of the fits with and without the two resonances in the signal yields are assigned as systematic uncertainties.

- To estimate the uncertainties associated with background contamination, alternative fits are performed by changing the number of background events with one standard deviation for various energy points. The differences in the signal yields are considered as the systematic uncertainties.

All these uncertainties are added in quadrature to provide the total systematic uncertainties of intermediate states (table 5).

6.2 Uncertainties for the measurements of $\sigma(e^+e^- \to \omega\pi^+\pi^-)$

The sources of systematic uncertainties associated with the Born cross section measurements include the tracking efficiency, photon detection, kinematic fit, π^0 mass window requirement, fit procedure, radiative correction, luminosity measurement, and branching fraction of $\omega \to \pi^+\pi^-\pi^0$. These sources are described as follows:

- The uncertainty due to the tracking efficiency is estimated as 1.0% per track [79].

- The uncertainty due to the photon detection is 1.0% per photon [80].

- The uncertainty associated with the kinematic fit originates from the inconsistency between the data and MC simulation of the track helix parameters. Following the procedure described in ref. [81], half of the difference in the detection efficiencies with and without the helix parameter correction is regarded the systematic uncertainty.

- The π^0 candidate is selected by requiring $|M_{\gamma\gamma} - 0.135| < 0.015\,\mathrm{GeV}/c^2$. By changing this requirement to $|M_{\gamma\gamma} - 0.135| < 0.018\,\mathrm{GeV}/c^2$ or $|M_{\gamma\gamma} - 0.135| < 0.013\,\mathrm{GeV}/c^2$, the larger difference in the measured cross section is considered as systematic uncertainty.

$\sqrt{s}$ (GeV)	Trk	ϵ_γ	4C	π^0	ISR	SS	BS	Fit	$\mathcal{L}$	Br	Δ_{MC}	Model	Total
2.0000	4.0	2.0	1.1	1.2	1.0	1.9	0.1	0.2	1.0	0.8	0.2	1.5	5.6
2.0500	4.0	2.0	1.1	1.0	1.0	2.0	0.6	0.3	1.0	0.8	0.2	1.3	5.6
2.1000	4.0	2.0	1.2	1.2	1.0	1.4	0.1	0.5	1.0	0.8	0.2	0.7	5.3
2.1250	4.0	2.0	1.1	1.1	1.0	1.7	0.1	0.3	1.0	0.8	0.2	0.9	5.4
2.1500	4.0	2.0	1.1	2.0	1.0	3.5	0.2	0.5	1.0	0.8	0.2	1.2	6.5
2.1750	4.0	2.0	1.1	0.3	1.0	1.4	0.3	0.7	1.0	0.8	0.2	0.6	5.2
2.2000	4.0	2.0	1.0	1.1	1.0	1.0	0.4	0.1	1.0	0.8	0.2	1.0	5.2
2.2324	4.0	2.0	1.1	0.9	1.0	0.9	0.9	1.9	1.0	0.8	0.2	0.4	5.5
2.3094	4.0	2.0	1.3	1.0	1.0	1.7	0.3	2.4	1.0	0.8	0.2	0.8	5.9
2.3864	4.0	2.0	1.4	0.7	1.0	0.8	0.1	0.2	1.0	0.8	0.3	1.0	5.2
2.3960	4.0	2.0	1.2	0.2	1.0	1.8	0.9	0.9	1.0	0.8	0.3	0.3	5.4
2.6444	4.0	2.0	1.1	0.4	1.0	1.7	0.7	0.9	1.0	0.8	0.3	0.5	5.3
2.6464	4.0	2.0	1.3	0.4	1.0	1.8	1.1	1.1	1.0	0.8	0.3	1.3	5.6
2.9000	4.0	2.0	1.6	2.0	1.0	1.5	0.5	0.2	1.0	0.8	0.3	0.5	5.7
2.9500	4.0	2.0	1.5	2.0	1.0	3.5	0.4	0.6	1.0	0.8	0.3	0.5	6.5
2.9810	4.0	2.0	1.5	2.0	1.0	2.0	0.3	0.2	1.0	0.8	0.3	0.8	5.9
3.0000	4.0	2.0	1.4	3.0	1.0	3.0	0.6	0.7	1.0	0.8	0.3	0.7	6.7
3.0200	4.0	2.0	1.5	1.0	1.0	2.5	0.5	0.2	1.0	0.8	0.3	1.0	5.8
3.0800	4.0	2.0	1.3	2.0	1.0	4.5	0.8	0.6	1.0	0.8	0.4	0.9	7.2

Table 6. Systematic uncertainties (in unit of %) of the $e^+e^- \to \omega\pi^+\pi^-$ cross section measurements at various energy points $(\sqrt{s})$. The main sources are from track efficiency (Trk), photon detection efficiency (ϵ_γ), 4C kinematic fit (4C), π^0 mass window (π^0), ISR effect, signal shape (SS) and background shape (BS), fit range (Fit), luminosity measurement ($\mathcal{L}$), ω decay branching fraction (Br), MC statistics (Δ_{MC}), and MC model. Meanwhile, the total uncertainty for each point (Total) is obtained by summing the individual contributions in quadrature.

- The uncertainties due to the choices of signal shape, background shape, and fit range are estimated by varying the signal function from the Breit-Wigner to the MC simulated shape convolved with a Gaussian resolution function. Another technique is varying the background function from the second-order to third-order Chebychev polynomial and by extending the fit range from (0.65, 0.89) GeV/c^2 to (0.64, 0.90) GeV/c^2. The differences in the signal yields are considered as systematic uncertainty.

- The ISR correction factor is calculated with the line shape of Born cross sections, which is smoothed by fitting the cross section distribution with five Gaussian functions. The signal MC samples with the ISR effect are generated according to the input line shape. Using the updated MC samples, we re-estimate the efficiency and ISR correction factor and then update the cross section. Iterations are performed un-

til the results are stable. Finally, the difference between the last two iterations, 1.0%, is considered the corresponding systematic uncertainty for all the energy points.

- The integrated luminosities of these data sets are measured using large angle Bhabha scattering events, with a uncertainty about 1.0% [82] is propagated to the cross section measurements. The uncertainty in $Br(\omega \to \pi^+\pi^-\pi^0)$ is quoted as 0.8% from the PDG [20].

- The uncertainty from the MC statistics is estimated by the number of generated events, calculated by $\Delta_{\mathrm{MC}} = \sqrt{(1-\epsilon)/\epsilon}/\sqrt{N}$, where $N = 1000000$ is the number of generated events at each energy points.

- The uncertainty due to the PWA MC model is investigated by smearing masses and widths of intermediate states per event within $\pm 1\sigma$, assuming that they follow Gaussian distribution. The difference in the detection efficiencies is considered the systematic uncertainty, which is about 1%. The effect due to the insignificant intermediate states, such as $\rho(1450)$ and $\rho(1570)$, is investigated by adding them to the nominal fit. Moreover, the difference in the detection efficiencies with and without these two intermediate states is regarded the systematic uncertainty, which varies from 0.2% to 1% depending on the energy point. The total uncertainty due to the MC model is obtained by adding these uncertainties in quadrature.

The systematic uncertainties for all energy points are listed in table 6. These uncertainties are assumed independent and summed in quadrature.

7 Fit to the line shapes

7.1 Line shape of $e^+e^- \to \omega\pi^+\pi^-$

The measured Born cross sections are shown in figure 8, where a clear structure is observed around 2.25 GeV. A minimized χ^2 fit incorporating the correlated and uncorrelated uncertainties is performed for the measured cross section with the following function:

$$\sigma^B(\sqrt{s}) = |\sigma_{\mathrm{r}}(\sqrt{s})e^{i\phi} + \sigma_{\mathrm{c}}(\sqrt{s})|^2, \tag{7.1}$$

where ϕ is the phase of the resonance structure relative to the continuum components and $\sigma_{\mathrm{r}}(\sqrt{s})$ and $\sigma_{\mathrm{c}}(\sqrt{s})$ are the cross sections for the resonance and continuum components, respectively. The resonant component $\sigma_{\mathrm{r}}(\sqrt{s})$ is parameterized as

$$\sigma_{\mathrm{r}}(\sqrt{s}) = \frac{m_r}{\sqrt{s}} \frac{\sqrt{12\pi C \Gamma_r^{ee} Br \Gamma_r}}{s - m_r^2 + im_r\Gamma_r} \sqrt{\frac{P(\sqrt{s})}{P(m_r)}}, \tag{7.2}$$

where m_r and Γ_r are the mass and width of the resonant structure near 2.25 GeV, respectively. Parameter $\Gamma_r^{ee} \cdot Br$ is the product of the partial width of the resonance decaying to the e^+e^- and the branching fraction to the $\omega\pi^+\pi^-$ final state. m_r, Γ_r and $\Gamma_r^{ee} \cdot Br$ are free

Parameter	Solution I	Solution II
m_r (MeV/c^2)	2250 $\pm$ 25	
Γ_r (MeV)	125 $\pm$ 23	
$\Gamma_r^{ee} \cdot Br$(eV)	0.9 $\pm$ 0.4	52.9 $\pm$ 17.0
ϕ (rad.)	2.4 $\pm$ 0.3	$-1.8 \pm$ 0.1
$a(10^3)$(pb$^{1/2}$)	1.1 $\pm$ 0.2	
b	4.4 $\pm$ 0.1	
Significance	10.3σ	

Table 7. Resonance parameters obtained in the fit to the $e^+e^- \to \omega\pi^+\pi^-$ cross section. The uncertainties are statistical only.

parameters in the fit. C is a conversion constant that equals to 3.893×10^5 nb·GeV^2 [18]. The continuum component is parameterized as

$$\sigma_c(\sqrt{s}) = \frac{a\sqrt{P(\sqrt{s})}}{\sqrt{s}^b}, \tag{7.3}$$

where a and b are free parameters and $P(\sqrt{s})$ is the phase factor. For the two-body process, $P(\sqrt{s})$ is taken as $p/\sqrt{s}$, where p is the magnitude of the momentum for one of the two particles. For the three-body final state of $\omega\pi^+\pi^-$,

$$P(\sqrt{s}) = \frac{1}{4s} \int_{2m_\pi}^{\sqrt{s}-m_\omega} \sqrt{(m_{\pi^+\pi^-}^2 - 4m_\pi^2)[s - (m_{\pi^+\pi^-} + m_\omega)^2][s - (m_{\pi^+\pi^-} - m_\omega)^2]} dm_{\pi^+\pi^-}, \tag{7.4}$$

where m_ω and $m_{\pi^+\pi^-}$ are the mass of ω particle and the invariant mass of $\pi^+\pi^-$, respectively. The results of the fits to the measured cross section are shown in figure 8. The data points of the BaBar experiment are plotted to overlap for comparison. The fit has two solutions with equally good fit quality and identical mass and width of the resonance, but with different phases and $\Gamma_r^{ee} \cdot Br$. We observe a structure around 2.25 GeV, denoted as $X(2230)$. The statistical significance of $X(2230)$ is 10.3σ, which is determined from the change in the χ^2 value with and without it in the fit versus the change of the number of degrees of freedom. The best fit provides a fit quality of χ^2/n.d.f = 20.6/13. The fit parameters of the two solutions are listed in table 7. Due to the interference effect, the parameter b is fitted as $b = 4.4 \pm 0.1$ in both two solutions. Note that this is different from the single virtual photon contribution where $b = 1$.

To estimate the systematic uncertainties for the resonant parameters, an alternative fit is performed by parameterizing the continuum component with an exponential function [83] to determine the uncertainties associated with the continuum component:

$$\sigma_c(\sqrt{s}) = \sqrt{P(\sqrt{s})e^{p_0 u}p_1}, \tag{7.5}$$

where p_0 and p_1 are float parameters and $u = \sqrt{s} - (2m_\pi + m_\omega)$, which the masses of m_π and m_ω take from the PDG [20]. The differences of the results between the alternative and

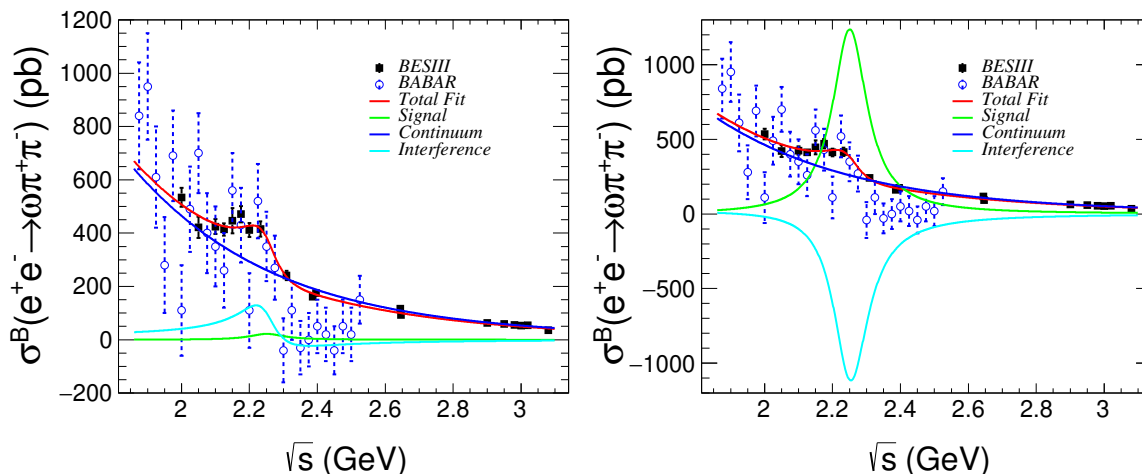**Figure 8**. Fits to the measured $e^+e^- \to \omega\pi^+\pi^-$ cross sections. The dots with error bars are the results obtained in the work, where the error bars include both statistical and systematic uncertainties. Circles with error bars (hatched line) are the results of the BaBar experiment. The red solid curve is the total fit result. The blue solid curve represents the continuum component, the green curve stands for the resonant component, and the cyan line is the interference of the two components. The two plots are the results of Solutions I (left) and II (right), respectively.

nominal fits are considered the systematic uncertainties for resonant parameters. Further, the systematic uncertainties associated with the signal model are investigated by using a relativistic Breit-Wigner function with the energy-dependent width. Their differences are found to be negligible. Eventually, the mass and width of the resonance are determined to be $m_r = 2250 \pm 25 \pm 27\,\mathrm{MeV}/c^2$ and $\Gamma_r = 125 \pm 43 \pm 15\,\mathrm{MeV}$, respectively. In addition, the $\Gamma_r^{ee} \cdot Br$ is $0.9 \pm 0.4 \pm 0.4\,\mathrm{eV}$ or $52.9 \pm 17.0 \pm 13.1\,\mathrm{eV}$ for the two solutions, where the first and second uncertainties are statistical and systematic, respectively.

7.2 Cross section of $e^+e^- \to \omega\pi\pi$

The Born cross sections for the $e^+e^- \to \omega\pi^+\pi^-$ measured in this work are consistent with that for the $e^+e^- \to \omega\pi^0\pi^0$ obtained in ref. [52] within a factor of 2 given their uncertainties. Therefore, the pion production in the $e^+e^- \to \omega\pi\pi$ process complies with the SU(3)-flavor symmetry. The summed cross sections at various energy points are listed in table 8. We fit the $e^+e^- \to \omega\pi\pi$ cross sections with the same method as in section 7.1 (see figure 9). The resultant parameters are obtained and tabulated in table 9. After considering the systematic uncertainty, the mass and width of X(2230) are obtained as $2232 \pm 19 \pm 27\,\mathrm{MeV}/c^2$ and $91 \pm 53 \pm 20\,\mathrm{MeV}$, respectively. The $\Gamma_r^{ee} \cdot Br$ is $0.9 \pm 0.5 \pm 0.2\,\mathrm{eV}$ and $61.1 \pm 32.1 \pm 15.4\,\mathrm{eV}$ for the two solutions. The statistical significance of the structure is 7.6σ.

We also compute the contribution of our cross section $\sigma^{\mathrm{Born}}(e^+e^- \to \omega\pi\pi)$ to the hadronic contribution of $(g-2)_\mu$,

$$a_\mu^{\omega\pi\pi} = \frac{1}{4\pi^3} \int_{(2.000\ \mathrm{GeV})^2}^{(3.080\ \mathrm{GeV})^2} ds' K(s')\sigma_{\omega\pi\pi}^{\mathrm{Born}}, \tag{7.6}$$

$\sqrt{s}$ (GeV)	Cross section (pb)	$\sqrt{s}$	Cross section (pb)
2.0000	$831.2 \pm 28.2 \pm 36.1$	2.3960	$251.6 \pm 6.2 \pm 10.9$
2.0500	$697.6 \pm 45.8 \pm 30.1$	2.6444	$176.6 \pm 7.2 \pm 7.5$
2.1000	$642.7 \pm 23.1 \pm 27.3$	2.6464	$148.0 \pm 6.4 \pm 6.5$
2.1250	$624.8 \pm 7.5 \pm 26.6$	2.9000	$88.40 \pm 2.8 \pm 4.0$
2.1500	$653.0 \pm 49.0 \pm 32.4$	2.9500	$79.70 \pm 8.0 \pm 4.2$
2.1750	$698.9 \pm 25.1 \pm 29.1$	2.9810	$85.70 \pm 7.4 \pm 3.9$
2.2000	$641.4 \pm 21.2 \pm 26.5$	3.0000	$68.20 \pm 6.5 \pm 3.7$
2.2324	$601.2 \pm 21.4 \pm 26.3$	3.0200	$69.70 \pm 6.2 \pm 3.4$
2.3096	$343.7 \pm 12.9 \pm 16.1$	3.0800	$47.90 \pm 2.2 \pm 2.8$
2.3864	$249.0 \pm 11.2 \pm 10.3$		

Table 8. Cross sections of $e^+e^- \to \omega\pi\pi$, where the first and second uncertainties are statistical and systematic, respectively.

Parameter	Solution I	Solution II
m_r (MeV/c^2)	2232 ± 19	
Γ_r (MeV)	93 ± 53	
$\Gamma_r^{ee} \cdot Br$(eV)	0.9 ± 0.5	61.1 ± 32.1
ϕ (rad)	2.4 ± 0.3	-1.7 ± 0.1
$a(10^3)$(pb$^{1/2}$)	1.7 ± 0.2	
b	4.6 ± 0.1	
Significance	7.6σ	

Table 9. Resonance parameters obtained in the fit to the $e^+e^- \to \omega\pi\pi$ cross section. The uncertainties are statistical only.

where $K(s')$ is the kernel function [74]. Our result, $a_\mu^{\omega\pi\pi}=(2.213 \pm 0.106 \pm 0.149)\times 10^{-10}$, is the first measurement for the $e^+e^- \to \omega\pi\pi$ process in this energy region.

7.3 $X(2230)$ decays via intermediate states

Using the measured Born cross sections via the intermediate states as tabulated in table 5, we perform a simultaneous fit to the measured cross sections σ_i^{exp} with $i = 1, 2, \ldots, 5$ for the modes $\omega f_0(500)$, $\omega f_0(980)$, $\omega f_0(1370)$, $\omega f_2(1270)$, and $b_1(1235)\pi$, respectively. At the energy point $\sqrt{s}$, the cross section for the mode i is described by

$$\sigma_i^{\text{fit}}(\sqrt{s}) = |\sigma_{\text{r}}e^{i\phi}(\sqrt{s},i) + \sigma_{\text{c}}(\sqrt{s},i)|^2 \tag{7.7}$$

Where, σ_{r} and σ_{c} are given by eqs. (7.2) and (7.3) except that the phase space factor is replaced by that of the two-body decay. Considering the error correlations among these
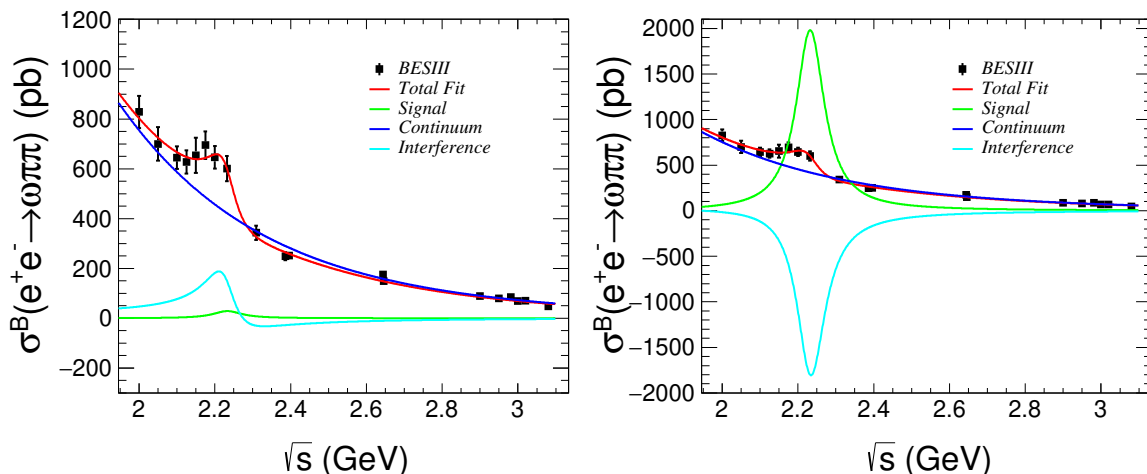
Figure 9. Fits to the cross sections of $e^+e^- \to \omega\pi\pi$. The dots with error bars are the results combined from this work and ref. [52], where the error bars include both statistical and systematic uncertainties. The red solid curves are the total fit results, the blue solid curves represent the continuum components, the green curves denote the resonant components, and the cyan line are the interference of the two components. The two plots are the results of Solutions I (left) and II (right), respectively.

five modes, the χ^2 function is minimized, which is defined by

$$\chi^2 = \sum_{\sqrt{s}} \Sigma^T V^{-1} \Sigma, \text{ with}$$

$$\Sigma^T = (\sigma_1^{\text{exp}} - \sigma_1^{\text{fit}}, \sigma_2^{\text{exp}} - \sigma_2^{\text{fit}}, \sigma_3^{\text{exp}} - \sigma_3^{\text{fit}}, \sigma_4^{\text{exp}} - \sigma_4^{\text{fit}}, \sigma_5^{\text{exp}} - \sigma_5^{\text{fit}}), \tag{7.8}$$

where V is a covariance matrix with element $V_{ij} = \rho_{ij}\sigma_i\sigma_j$ and ρ_{ij} is a correlation coefficient and determined by the errors of interference between modes i and j. We take $\rho_{ij} = 1$ if $i = j$. The sum over $\sqrt{s}$ runs over all energy points involved in the fit.

Figure 10 shows results of the simultaneous fit to these five intermediate modes. In the fit, the state $X(2230)$ is assumed as a vector meson, and its mass and width is $2200 \pm 11 \pm 17 \,\text{MeV}/c^2$ and $74 \pm 20 \pm 24 \,\text{MeV}$, respectively. Here, the systematic uncertainties of the mass and width are determined by using the same method as in section 7.1. The statistical significance of this structure is about 7.9σ. The resultant values of $\Gamma_r^{ee} \cdot Br$ are tabulated in table 10. Here, Γ_r^{ee} is the partial width of the $X(2230)$ decaying to e^+e^-, and Br is the branching fraction for the $X(2230)$ decaying to the final state $\omega\pi\pi$. Two solutions are found with equally good fit quality. No structure around $2.25 \,\text{GeV}$ is observed in the non-resonant process, as shown in figure 10(f), indicating that the vector meson favors the intermediate decay.

8 Conclusion and discussion

In summary, the Born cross sections of the $e^+e^- \to \omega\pi^+\pi^-$ process were measured using $647 \,\text{pb}^{-1}$ data samples collected with the BESIII detector at 19 c.m. energies from

	Solution I	Solution II
$e^+e^- \to f$	$\Gamma_r^{ee} \cdot Br$ (eV)	$\Gamma_r^{ee} \cdot Br$ (eV)
$\omega f_0(500)$	2.9 ± 2.5	1.2 ± 0.5
$\omega f_0(980)$	5.9 ± 5.0	3.2 ± 1.0
$\omega f_0(1370)$	6.4 ± 5.4	3.1 ± 1.0
$\omega f_2(1270)$	2.5 ± 2.1	1.1 ± 0.6
$b_1(1235)\pi$	1.1 ± 1.0	0.2 ± 0.2

Table 10. $\Gamma_r^{ee} \cdot Br$ values from the simultaneous fit to the cross sections for the five intermediate modes, where the uncertainties are statistical only.
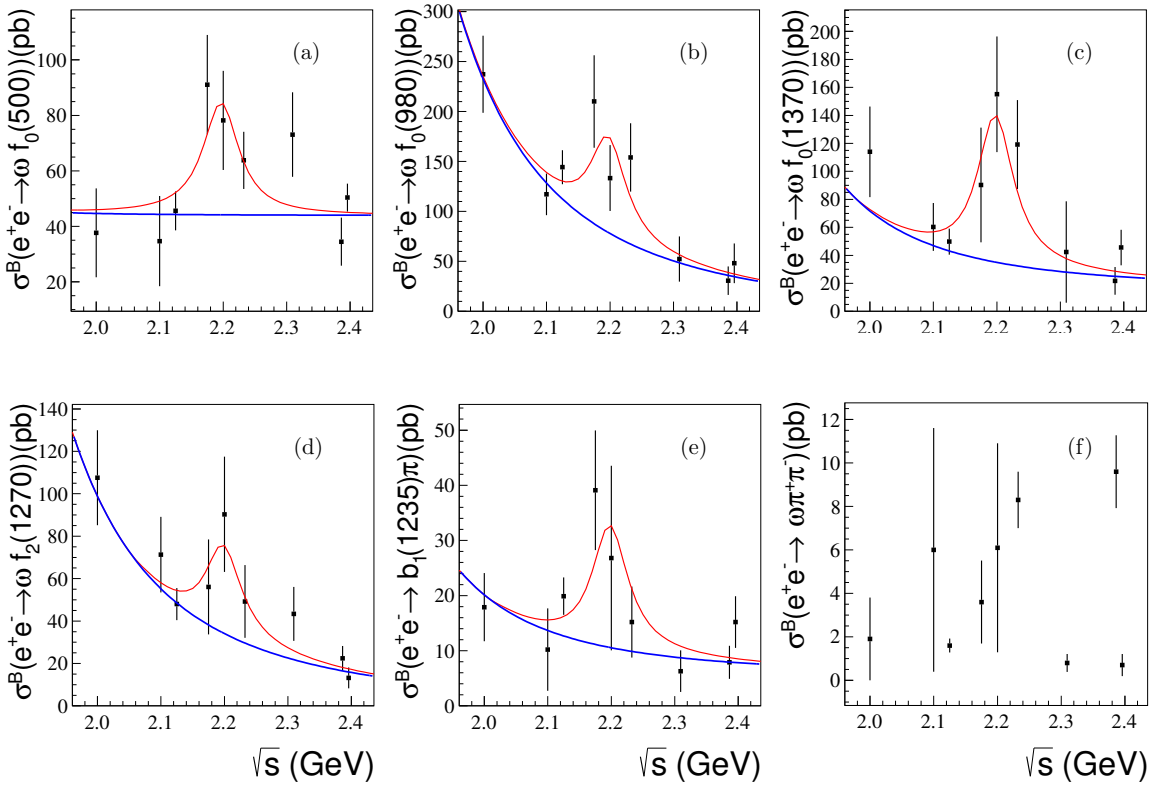
Figure 10. Fits to the intermediate processes of $e^+e^- \to \omega f_0(500)$ (a), $\omega f_0(980)$ (b), $\omega f_0(1370)$ (c), $\omega f_2(1270)$ (d), $b_1(1235)\pi$ (e). Points with error bars are the measured Born cross sections, the red curves are the total fit results, and the blue curves denote the contributions of non-resonant processes. Plot (f) displays the contribution from the phase space process $e^+e^- \to \omega\pi^+\pi^-$.

2.000 GeV to 3.080 GeV. The precision of the measured cross sections are improved by a factor of 3 with respect to the previous measurement [18]. The resonance $X(2230)$ is observed with a significance of 7.6 σ and thereby confirms the structure near 2.25 GeV observed by BaBar [18] and BESIII [52]. The energy dependence of the total cross section for $e^+e^- \rightarrow \omega\pi^+\pi^-$ and $\omega\pi^0\pi^0$ is shown in figure 9. From the fit to the $e^+e^- \rightarrow \omega\pi\pi$ cross sections, we obtained the mass and width of $X(2230)$ as $2232 \pm 19 \pm 27\,\mathrm{MeV}/c^2$ and $93 \pm 53 \pm 20\,\mathrm{MeV}$, respectively. The fitted $\Gamma_r^{ee} \cdot Br$ values are $0.9 \pm 0.5 \pm 0.2\,\mathrm{eV}$ and $61.1 \pm 32.1 \pm 15.4\,\mathrm{eV}$ depending on the interference pattern. We also fit the Born cross section of the intermediate processes, such as $e^+e^- \rightarrow \omega f_0(500)$, $\omega f_0(980)$, $\omega f_0(1370)$, $\omega f_2(1270)$, and $b_1(1235)\pi$, with the results presented in figure 10. Precision measurement of the cross sections of these intermediate subprocesses will help to reveal the properties and nature of the structure. For the process $e^+e^- \rightarrow \omega\pi\pi$, we computed its hadronic contribution of the cross section to $(g-2)_\mu$ and found that its contribution is small in the energy region between 2.000 GeV and 3.080 GeV.

References

[1] BESIII collaboration, *Observation of a charged charmoniumlike structure in $e^+e^- \to \pi^+\pi^- J/\psi$ at $\sqrt{s} = 4.26\,GeV$, Phys. Rev. Lett. **110** (2013) 252001* [arXiv:1303.5949] [INSPIRE].

[2] BESIII collaboration, *Observation of a charged charmoniumlike structure $Z_c(4020)$ and search for the $Z_c(3900)$ in $e^+e^- \to \pi^+\pi^- h_c$, Phys. Rev. Lett. **111** (2013) 242001* [arXiv:1309.1896] [INSPIRE].

[3] BESIII collaboration, *Observation of a charged $(D\bar{D}^*)^\pm$ mass peak in $e^+e^- \to \pi D\bar{D}^*$ at $\sqrt{s} = 4.26\,GeV$, Phys. Rev. Lett. **112** (2014) 022001* [arXiv:1310.1163] [INSPIRE].

[4] BESIII collaboration, *Observation of a charged charmoniumlike structure in $e^+e^- \to (D^*\bar{D}^*)^\pm\pi^\mp$ at $\sqrt{s} = 4.26\,GeV$, Phys. Rev. Lett. **112** (2014) 132001* [arXiv:1308.2760] [INSPIRE].

[5] BESIII collaboration, *Observation of $e^+e^- \to \pi^0\pi^0 h_c$ and a neutral charmoniumlike structure $Z_c(4020)^0$, Phys. Rev. Lett. **113** (2014) 212002* [arXiv:1409.6577] [INSPIRE].

[6] BESIII collaboration, *Observation of $Z_c(3900)^0$ in $e^+e^- \to \pi^0\pi^0 J/\psi$, Phys. Rev. Lett. **115** (2015) 112003* [arXiv:1506.06018] [INSPIRE].

[7] BESIII collaboration, *Observation of a neutral charmoniumlike state $Z_c(4025)^0$ in $e^+e^- \to (D^*\bar{D}^*)^0\pi^0$, Phys. Rev. Lett. **115** (2015) 182002* [arXiv:1507.02404] [INSPIRE].

[8] BESIII collaboration, *Observation of a neutral structure near the $D\bar{D}^*$ mass threshold in $e^+e^- \to (D\bar{D}^*)^0\pi^0$ at $\sqrt{s} = 4.226$ and $4.257\,GeV$, Phys. Rev. Lett. **115** (2015) 222002* [arXiv:1509.05620] [INSPIRE].

[9] BELLE collaboration, *Study of $e^+e^- \to \pi^+\pi^- J/\psi$ and observation of a charged charmoniumlike state at Belle, Phys. Rev. Lett. **110** (2013) 252002* [*Erratum ibid.* **111** (2013) 019901] [arXiv:1304.0121] [INSPIRE].

[10] T. Xiao, S. Dobbs, A. Tomaradze and K.K. Seth, *Observation of the charged hadron $Z_c^\pm(3900)$ and evidence for the neutral $Z_c^0(3900)$ in $e^+e^- \to \pi\pi J/\psi$ at $\sqrt{s} = 4170\,MeV$, Phys. Lett. B **727** (2013) 366* [arXiv:1304.3036] [INSPIRE].

[11] BESIII collaboration, *Observation of a near-threshold structure in the K^+ recoil-mass spectra in $e^+e^- \to K^+(D_s^- D^{*0} + D_s^{*-} D^0)$, Phys. Rev. Lett. **126** (2021) 102001* [arXiv:2011.07855] [INSPIRE].

[12] BESIII collaboration, *Evidence for a neutral near-threshold structure in the K_S^0 recoil-mass spectra in $e^+e^- \to K_S^0 D_s^+ D^{*-}$ and $e^+e^- \to K_S^0 D_s^{*+} D^-$, Phys. Rev. Lett. **129** (2022) 112003* [arXiv:2204.13703] [INSPIRE].

[13] MUON G-2 collaboration, *Measurement of the positive muon anomalous magnetic moment to $0.46\,ppm$, Phys. Rev. Lett. **126** (2021) 141801* [arXiv:2104.03281] [INSPIRE].

[14] M. Davier, *The hadronic contribution to $(g-2)_\mu$, Nucl. Phys. B Proc. Suppl. **169** (2007) 288* [hep-ph/0701163] [INSPIRE].

[15] T. Aoyama et al., *The anomalous magnetic moment of the muon in the Standard Model, Phys. Rept. **887** (2020) 1* [arXiv:2006.04822] [INSPIRE].

[16] M. Davier, A. Hoecker, B. Malaescu and Z. Zhang, *Reevaluation of the hadronic contributions to the muon $g-2$ and to $\alpha(M_Z^2)$, Eur. Phys. J. C **71** (2011) 1515* [*Erratum ibid.* **72** (2012) 1874] [arXiv:1010.4180] [INSPIRE].

[17] M. Golterman, *Theory review for hadronic corrections to g − 2*, in 20th *conference on flavor physics and CP-violation*, (2022) [`arXiv:2208.05560`] [InSPIRE].

[18] BaBar collaboration, *The $e^+e^- \to 2(\pi^+\pi^-)\pi^0$, $2(\pi^+\pi^-)\eta$, $K^+K^-\pi^+\pi^-\pi^0$ and $K^+K^-\pi^+\pi^-\eta$ cross section measured with initial-state radiation*, *Phys. Rev. D* **76** (2007) 092005 [*Erratum ibid.* **77** (2008) 119902] [`arXiv:0708.2461`] [InSPIRE].

[19] BaBar collaboration, *Resonances in e^+e^- annihilation near* 2.2 GeV, *Phys. Rev. D* **101** (2020) 012011 [`arXiv:1912.04512`] [InSPIRE].

[20] Particle Data Group collaboration, *Review of particle physics*, *PTEP* **2020** (2020) 083C01 [InSPIRE].

[21] G.J. Ding and M.L. Yan, *Y(2175): distinguish hybrid state from higher quarkonium*, *Phys. Lett. B* **657** (2007) 49 [`hep-ph/0701047`] [InSPIRE].

[22] X. Wang, Z.F. Sun, D.Y. Chen, X. Liu and T. Matsuki, *Non-strange partner of strangeonium-like state Y(2175)*, *Phys. Rev. D* **85** (2012) 074024 [`arXiv:1202.4139`] [InSPIRE].

[23] S.S. Afonin and I.V. Pusenkov, *Universal description of radially excited heavy and light vector mesons*, *Phys. Rev. D* **90** (2014) 094020 [`arXiv:1411.2390`] [InSPIRE].

[24] C.Q. Pang, *Excited states of φ meson*, *Phys. Rev. D* **99** (2019) 074015 [`arXiv:1902.02206`] [InSPIRE].

[25] C.G. Zhao, G.Y. Wang, G.N. Li, E. Wang and D.M. Li, *φ(2170) production in the process $\gamma p \to \eta\phi p$*, *Phys. Rev. D* **99** (2019) 114014 [`arXiv:1904.08569`] [InSPIRE].

[26] Q. Li, L.C. Gui, M.S. Liu, Q.F. Lü and X.H. Zhong, *Mass spectrum and strong decays of strangeonium in a constituent quark model*, *Chin. Phys. C* **45** (2021) 023116 [`arXiv:2004.05786`] [InSPIRE].

[27] G.J. Ding and M.L. Yan, *A candidate for 1^{--} strangeonium hybrid*, *Phys. Lett. B* **650** (2007) 390 [`hep-ph/0611319`] [InSPIRE].

[28] J. Ho, R. Berg, T.G. Steele, W. Chen and D. Harnett, *Is the Y(2175) a strangeonium hybrid meson?*, *Phys. Rev. D* **100** (2019) 034012 [`arXiv:1905.12779`] [InSPIRE].

[29] Z.G. Wang, *Analysis of the Y(2175) as a tetraquark state with QCD sum rules*, *Nucl. Phys. A* **791** (2007) 106 [`hep-ph/0610171`] [InSPIRE].

[30] H.X. Chen, X. Liu, A. Hosaka and S.L. Zhu, *The Y(2175) state in the QCD sum rule*, *Phys. Rev. D* **78** (2008) 034012 [`arXiv:0801.4603`] [InSPIRE].

[31] N.V. Drenska, R. Faccini and A.D. Polosa, *Higher tetraquark particles*, *Phys. Lett. B* **669** (2008) 160 [`arXiv:0807.0593`] [InSPIRE].

[32] C. Deng, J. Ping, F. Wang and T. Goldman, *Tetraquark state and multibody interaction*, *Phys. Rev. D* **82** (2010) 074001 [InSPIRE].

[33] H.W. Ke and X.Q. Li, *Study of the strong decays of φ(2170) and the future charm-tau factory*, *Phys. Rev. D* **99** (2019) 036014 [`arXiv:1810.07912`] [InSPIRE].

[34] S.S. Agaev, K. Azizi and H. Sundu, *Nature of the vector resonance Y(2175)*, *Phys. Rev. D* **101** (2020) 074012 [`arXiv:1911.09743`] [InSPIRE].

[35] R.R. Dong, N. Su, H.X. Chen, E.L. Cui and Z.Y. Zhou, *QCD sum rule studies on the $ss\bar{s}\bar{s}$ tetraquark states of $J^{PC} = 0^{-+}$*, *Eur. Phys. J. C* **80** (2020) 749 [`arXiv:2003.07670`] [InSPIRE].

[36] F.X. Liu, M.S. Liu, X.H. Zhong and Q. Zhao, *Fully-strange tetraquark $ss\bar{s}\bar{s}$ spectrum and possible experimental evidence*, *Phys. Rev. D* **103** (2021) 016016 [arXiv:2008.01372] [INSPIRE].

[37] E. Klempt and A. Zaitsev, *Glueballs, hybrids, multiquarks. Experimental facts versus QCD inspired concepts*, *Phys. Rept.* **454** (2007) 1 [arXiv:0708.4016] [INSPIRE].

[38] L. Zhao, N. Li, S.L. Zhu and B.S. Zou, *Meson-exchange model for the $\Lambda\bar{\Lambda}$ interaction*, *Phys. Rev. D* **87** (2013) 054034 [arXiv:1302.1770] [INSPIRE].

[39] C. Deng, J. Ping, Y. Yang and F. Wang, *Baryonia and near-threshold enhancements*, *Phys. Rev. D* **88** (2013) 074007 [arXiv:1306.6725] [INSPIRE].

[40] Y. Dong, A. Faessler, T. Gutsche, Q. Lü and V.E. Lyubovitskij, *Selected strong decays of $\eta(2225)$ and $\phi(2170)$ as $\Lambda\bar{\Lambda}$ bound states*, *Phys. Rev. D* **96** (2017) 074027 [arXiv:1705.09631] [INSPIRE].

[41] Y. Yang, D.Y. Chen and Z. Lu, *Electromagnetic form factors of Λ hyperon in the vector meson dominance model*, *Phys. Rev. D* **100** (2019) 073007 [arXiv:1902.01242] [INSPIRE].

[42] A. Martinez Torres, K.P. Khemchandani, L.S. Geng, M. Napsuciale and E. Oset, *The $X(2175)$ as a resonant state of the $\phi K\bar{K}$ system*, *Phys. Rev. D* **78** (2008) 074031 [arXiv:0801.3635] [INSPIRE].

[43] S. Gomez-Avila, M. Napsuciale and E. Oset, *ϕK^+K^- production in electron-positron annihilation*, *Phys. Rev. D* **79** (2009) 034018 [arXiv:0711.4147] [INSPIRE].

[44] BESIII collaboration, *Measurement of $e^+e^- \to K^+K^-$ cross section at $\sqrt{s} = 2.00$–3.08 GeV*, *Phys. Rev. D* **99** (2019) 032001 [arXiv:1811.08742] [INSPIRE].

[45] BESIII collaboration, *Observation of a resonant structure in $e^+e^- \to K^+K^-\pi^0\pi^0$*, *Phys. Rev. Lett.* **124** (2020) 112001 [arXiv:2001.04131] [INSPIRE].

[46] BESIII collaboration, *Observation of a structure in $e^+e^- \to \phi\eta'$ at $\sqrt{s}$ from 2.05 to 3.08 GeV*, *Phys. Rev. D* **102** (2020) 012008 [arXiv:2003.13064] [INSPIRE].

[47] BESIII collaboration, *Observation of a resonant structure in $e^+e^- \to \omega\eta$ and another in $e^+e^- \to \omega\pi^0$ at center-of-mass energies between 2.00 and 3.08 GeV*, *Phys. Lett. B* **813** (2021) 136059 [arXiv:2009.08099] [INSPIRE].

[48] BESIII collaboration, *Cross section measurement of $e^+e^- \to K^0_S K^0_L$ at $\sqrt{s} = 2.00$–3.08 GeV*, *Phys. Rev. D* **104** (2021) 092014 [arXiv:2105.13597] [INSPIRE].

[49] BESIII collaboration, *Measurement of the Born cross sections for $e^+e^- \to \eta'\pi^+\pi^-$ at center-of-mass energies between 2.00 and 3.08 GeV*, *Phys. Rev. D* **103** (2021) 072007 [arXiv:2012.07360] [INSPIRE].

[50] BESIII collaboration, *Cross section measurements of $e^+e^- \to K^+K^-K^+K^-$ and ϕK^+K^- at center-of-mass energies from 2.10 to 3.08 GeV*, *Phys. Rev. D* **100** (2019) 032009 [arXiv:1907.06015] [INSPIRE].

[51] C.Q. Pang, Y.R. Wang, J.F. Hu, T.J. Zhang and X. Liu, *Study of the ω meson family and newly observed ω-like state $X(2240)$*, *Phys. Rev. D* **101** (2020) 074022 [arXiv:1910.12408] [INSPIRE].

[52] BESIII collaboration, *Measurement of the $e^+e^- \to \omega\pi^0\pi^0$ cross section at center-of-mass energies from 2.0 to 3.08 GeV*, *Phys. Rev. D* **105** (2022) 032005 [arXiv:2112.15076] [INSPIRE].

[53] BESIII collaboration, *Design and construction of the BESIII detector*, *Nucl. Instrum. Meth. A* **614** (2010) 345 [arXiv:0911.4960] [INSPIRE].

[54] C.H. Yu et al., *BEPCII performance and beam dynamics studies on luminosity*, in *Proceedings of the* 7th *Int. Particle Accelerator Conf.* IPAC2016, Busan, Korea (2016).

[55] BESIII collaboration, *Future physics programme of BESIII*, *Chin. Phys. C* **44** (2020) 040001 [arXiv:1912.05983] [INSPIRE].

[56] GEANT4 collaboration, *GEANT4 — a simulation toolkit*, *Nucl. Instrum. Meth. A* **506** (2003) 250 [INSPIRE].

[57] F. Campanario et al., *Standard Model radiative corrections in the pion form factor measurements do not explain the a_μ anomaly*, *Phys. Rev. D* **100** (2019) 076004 [arXiv:1903.10197] [INSPIRE].

[58] H. Czyż, J.H. Kühn and S. Tracz, *Nucleon form factors and final state radiative corrections to $e^+e^- \to p\bar{p}\gamma$*, *Phys. Rev. D* **90** (2014) 114021 [arXiv:1407.7995] [INSPIRE].

[59] R.G. Ping et al., *Tuning and validation of hadronic event generator for R value measurements in the tau-charm region*, *Chin. Phys. C* **40** (2016) 113002 [arXiv:1605.09208] [INSPIRE].

[60] R.G. Ping, *An exclusive event generator for e^+e^- scan experiments*, *Chin. Phys. C* **38** (2014) 083001 [arXiv:1309.3932] [INSPIRE].

[61] E.A. Kuraev and V.S. Fadin, *On radiative corrections to e^+e^- single photon annihilation at high-energy*, *Sov. J. Nucl. Phys.* **41** (1985) 466 [*Yad. Fiz.* **41** (1985) 733] [INSPIRE].

[62] B. Andersson and H.M. Hu, *Few body states in Lund string fragmentation model*, hep-ph/9910285 [INSPIRE].

[63] X. Zhou, S. Du, G. Li and C. Shen, *TopoAna: a generic tool for the event type analysis of inclusive Monte-Carlo samples in high energy physics experiments*, *Comput. Phys. Commun.* **258** (2021) 107540 [arXiv:2001.04016] [INSPIRE].

[64] LHCb collaboration, *Observation of $J/\psi p$ resonances consistent with pentaquark states in $\Lambda_b^0 \to J/\psi K^- p$ decays*, *Phys. Rev. Lett.* **115** (2015) 072001 [arXiv:1507.03414] [INSPIRE].

[65] BELLE collaboration, *Experimental constraints on the spin and parity of the $Z(4430)^+$*, *Phys. Rev. D* **88** (2013) 074026 [arXiv:1306.4894] [INSPIRE].

[66] H. Chen and R.G. Ping, *Coherent helicity amplitude for sequential decays*, *Phys. Rev. D* **95** (2017) 076010 [arXiv:1704.05184] [INSPIRE].

[67] S.M. Berman and M. Jacob, *Spin and parity analysis in two-step decay processes*, report number SLAC-0043, SLAC, Menlo Park, CA, U.S.A., May 1965 [INSPIRE].

[68] S.U. Chung, *A general formulation of covariant helicity coupling amplitudes*, *Phys. Rev. D* **57** (1998) 431 [INSPIRE].

[69] S.U. Chung, *Helicity coupling amplitudes in tensor formalism*, *Phys. Rev. D* **48** (1993) 1225 [*Erratum ibid.* **56** (1997) 4419] [INSPIRE].

[70] S.U. Chung and J. Friedrich, *Covariant helicity-coupling amplitudes: a new formulation*, *Phys. Rev. D* **78** (2008) 074027 [arXiv:0711.3143] [INSPIRE].

[71] F. James and M. Roos, *Minuit: a system for function minimization and analysis of the parameter errors and correlations*, *Comput. Phys. Commun.* **10** (1975) 343 [INSPIRE].

[72] BES collaboration, *The σ pole in $J/\psi \to \omega\pi^+\pi^-$*, *Phys. Lett. B* **598** (2004) 149 [hep-ex/0406038] [INSPIRE].

[73] BES collaboration, *Production of σ in $\psi(2S) \to \pi^+\pi^- J/\psi$*, *Phys. Lett. B* **645** (2007) 19 [hep-ex/0610023] [INSPIRE].

[74] S. Eidelman and F. Jegerlehner, *Hadronic contributions to $g - 2$ of the leptons and to the effective fine structure constant $\alpha(M_z^2)$*, *Z. Phys. C* **67** (1995) 585 [hep-ph/9502298] [INSPIRE].

[75] F. Jegerlehner, *Precision measurements of σ_{hadronic} for $\alpha_{\text{eff}}(E)$ at ILC energies and $(g - 2)_\mu$*, *Nucl. Phys. B Proc. Suppl.* **162** (2006) 22 [hep-ph/0608329] [INSPIRE].

[76] F. Jegerlehner, *The running fine structure constant $\alpha(E)$ via the Adler function*, *Nucl. Phys. B Proc. Suppl.* **181-182** (2008) 135 [arXiv:0807.4206] [INSPIRE].

[77] F. Jegerlehner, *Theoretical precision in estimates of the hadronic contributions to $(g - 2)_\mu$ and $\alpha_{\text{QED}}(M_Z)$*, *Nucl. Phys. B Proc. Suppl.* **126** (2004) 325 [hep-ph/0310234] [INSPIRE].

[78] F. Jegerlehner, *Hadronic vacuum polarization effects in $\alpha_{\text{em}}(M_Z)$*, in *Mini-workshop on electroweak precision data and the Higgs mass*, (2003), p. 97 [hep-ph/0308117] [INSPIRE].

[79] BESIII collaboration, *Search for a strangeonium-like structure Z_s decaying into $\phi\pi$ and a measurement of the cross section $e^+e^- \to \phi\pi\pi$*, *Phys. Rev. D* **99** (2019) 011101 [arXiv:1801.10384] [INSPIRE].

[80] BESIII collaboration, *Branching fraction measurements of χ_{c0} and χ_{c2} to $\pi^0\pi^0$ and $\eta\eta$*, *Phys. Rev. D* **81** (2010) 052005 [arXiv:1001.5360] [INSPIRE].

[81] BESIII collaboration, *Search for hadronic transition $\chi_{cJ} \to \eta_c\pi^+\pi^-$ and observation of $\chi_{cJ} \to K\bar{K}\pi\pi$*, *Phys. Rev. D* **87** (2013) 012002 [arXiv:1208.4805] [INSPIRE].

[82] BESIII collaboration, *Luminosity measurements for the R scan experiment at BESIII*, *Chin. Phys. C* **41** (2017) 063001 [arXiv:1702.04977] [INSPIRE].

[83] BESIII collaboration, *Precise measurement of the $e^+e^- \to \pi^+\pi^- J/\psi$ cross section at center-of-mass energies from 3.77 to 4.60 GeV*, *Phys. Rev. Lett.* **118** (2017) 092001 [arXiv:1611.01317] [INSPIRE].

The BESIII collaboration

M. Ablikim[1], M. N. Achasov[10,b], P. Adlarson[68], S. Ahmed[14], M. Albrecht[4], R. Aliberti[28], A. Amoroso[67A,67C], M. R. An[32], Q. An[64,50], X. H. Bai[58], Y. Bai[49], O. Bakina[29], R. Baldini Ferroli[23A], I. Balossino[24A], Y. Ban[39,h], V. Batozskaya[1,37], D. Becker[28], K. Begzsuren[26], N. Berger[28], M. Bertani[23A], D. Bettoni[24A], F. Bianchi[67A,67C], J. Bloms[61], A. Bortone[67A,67C], I. Boyko[29], R. A. Briere[5], A. Brueggemann[61], H. Cai[69], X. Cai[1,50], A. Calcaterra[23A], G. F. Cao[1,55], N. Cao[1,55], S. A. Cetin[54A], J. F. Chang[1,50], W. L. Chang[1,55], G. Chelkov[29,a], C. Chen[36], G. Chen[1], H. S. Chen[1,55], M. L. Chen[1,50], S. J. Chen[35], T. Chen[1], X. R. Chen[25], X. T. Chen[1], Y. B. Chen[1,50], Z. J. Chen[20,i], W. S. Cheng[67C], G. Cibinetto[24A], F. Cossio[67C], J. J. Cui[42], H. L. Dai[1,50], J. P. Dai[71], X. C. Dai[1,55], A. Dbeyssi[14], R. E. de Boer[4], D. Dedovich[29], Z. Y. Deng[1], A. Denig[28], I. Denysenko[29], M. Destefanis[67A,67C], F. De Mori[67A,67C], Y. Ding[33], J. Dong[1,50], L. Y. Dong[1,55], M. Y. Dong[1,50,55], X. Dong[69], S. X. Du[73], P. Egorov[29,a], Y. L. Fan[69], J. Fang[1,50], S. S. Fang[1,55], Y. Fang[1], R. Farinelli[24A], L. Fava[67B,67C], F. Feldbauer[4], G. Felici[23A], C. Q. Feng[64,50], J. H. Feng[51], K Fischer[62], M. Fritsch[4], C. D. Fu[1], Y. N. Gao[39,h], Yang Gao[64,50], I. Garzia[24A,24B], P. T. Ge[69], C. Geng[51], E. M. Gersabeck[59], A Gilman[62], K. Goetzen[11], L. Gong[33], W. X. Gong[1,50], W. Gradl[28], M. Greco[67A,67C], M. H. Gu[1,50], C. Y Guan[1,55], A. Q. Guo[22], A. Q. Guo[25], L. B. Guo[34], R. P. Guo[41], Y. P. Guo[9,g], A. Guskov[29,a], T. T. Han[42], W. Y. Han[32], X. Q. Hao[15], F. A. Harris[57], K. K. He[47], K. L. He[1,55], F. H. Heinsius[4], C. H. Heinz[28], Y. K. Heng[1,50,55], C. Herold[52], M. Himmelreich[11,e], T. Holtmann[4], G. Y. Hou[1,55], Y. R. Hou[55], Z. L. Hou[1], H. M. Hu[1,55], J. F. Hu[48,j], T. Hu[1,50,55], Y. Hu[1], G. S. Huang[64,50], K. X. Huang[51], L. Q. Huang[65], X. T. Huang[42], Y. P. Huang[1], Z. Huang[39,h], T. Hussain[66], N Hüsken[22,28], W. Imoehl[22], M. Irshad[64,50], S. Jaeger[4], S. Janchiv[26], Q. Ji[1], Q. P. Ji[15], X. B. Ji[1,55], X. L. Ji[1,50], Y. Y. Ji[42], H. B. Jiang[42], S. S. Jiang[32], X. S. Jiang[1,50,55], J. B. Jiao[42], Z. Jiao[18], S. Jin[35], Y. Jin[58], M. Q. Jing[1,55], T. Johansson[68], N. Kalantar-Nayestanaki[56], X. S. Kang[33], R. Kappert[56], M. Kavatsyuk[56], B. C. Ke[73], I. K. Keshk[4], A. Khoukaz[61], P. Kiese[28], R. Kiuchi[1], R. Kliemt[11], L. Koch[30], O. B. Kolcu[54A], B. Kopf[4], M. Kuemmel[4], M. Kuessner[4], A. Kupsc[37,68], M. G. Kurth[1,55], W. Kühn[30], J. J. Lane[59], J. S. Lange[30], P. Larin[14], A. Lavania[21], L. Lavezzi[67A,67C], Z. H. Lei[64,50], H. Leithoff[28], M. Lellmann[28], T. Lenz[28], C. Li[40], C. Li[36], C. H. Li[32], Cheng Li[64,50], D. M. Li[73], F. Li[1,50], G. Li[1], H. Li[64,50], H. Li[44], H. B. Li[1,55], H. J. Li[15], H. N. Li[48,j], J. L. Li[42], J. Q. Li[4], J. S. Li[51], Ke Li[1], L. J Li[1], L. K. Li[1], Lei Li[3], M. H. Li[36], P. R. Li[31,k,l], S. X. Li[9], S. Y. Li[53], T. Li[42], W. D. Li[1,55], W. G. Li[1], X. H. Li[64,50], X. L. Li[42], Xiaoyu Li[1,55], Z. Y. Li[51], H. Liang[27], H. Liang[1,55], H. Liang[64,50], Y. F. Liang[46], Y. T. Liang[25], G. R. Liao[12], L. Z. Liao[1,55], J. Libby[21], A. Limphirat[52], C. X. Lin[51], D. X. Lin[25], T. Lin[1], B. J. Liu[1], C. X. Liu[1], D. Liu[14,64], F. H. Liu[45], Fang Liu[1], Feng Liu[6], G. M. Liu[48,j], H. M. Liu[1,55], Huanhuan Liu[1], Huihui Liu[16], J. B. Liu[64,50], J. L. Liu[65], J. Y. Liu[1,55], K. Liu[1], K. Y. Liu[33], Ke Liu[17], L. Liu[64,50], M. H. Liu[9,g], P. L. Liu[1], Q. Liu[55], S. B. Liu[64,50], T. Liu[9,g], T. Liu[1,55], W. M. Liu[64,50], X. Liu[31,k,l], Y. Liu[31,k,l], Y. B. Liu[36], Z. A. Liu[1,50,55], Z. Q. Liu[42], X. C. Lou[1,50,55], F. X. Lu[51], H. J. Lu[18], J. D. Lu[1,55], J. G. Lu[1,50], X. L. Lu[1], Y. Lu[1], Y. P. Lu[1,50], Z. H. Lu[1], C. L. Luo[34], M. X. Luo[72], T. Luo[9,g], X. L. Luo[1,50], X. R. Lyu[55], Y. F. Lyu[36], F. C. Ma[33], H. L. Ma[1], L. L. Ma[42], M. M. Ma[1,55], Q. M. Ma[1], R. Q. Ma[1,55], R. T. Ma[55], X. X. Ma[1,55], X. Y. Ma[1,50], Y. Ma[39,h], F. E. Maas[14], M. Maggiora[67A,67C], S. Maldaner[4], S. Malde[62], Q. A. Malik[66], A. Mangoni[23B], Y. J. Mao[39,h], Z. P. Mao[1], S. Marcello[67A,67C], Z. X. Meng[58], J. G. Messchendorp[56,d], G. Mezzadri[24A], H. Miao[1], T. J. Min[35], R. E. Mitchell[22], X. H. Mo[1,50,55], N. Yu. Muchnoi[10,b], H. Muramatsu[60], S. Nakhoul[11,e], Y. Nefedov[29], F. Nerling[11,e], I. B. Nikolaev[10,b], Z. Ning[1,50], S. Nisar[8,m], S. L. Olsen[55], Q. Ouyang[1,50,55], S. Pacetti[23B,23C], X. Pan[9,g], Y. Pan[59], A. Pathak[1], A. Pathak[27], M. Pelizaeus[4], H. P. Peng[64,50], K. Peters[11,e], J. Pettersson[68], J. L. Ping[34], R. G. Ping[1,55], S. Plura[28], S. Pogodin[29], R. Poling[60],

V. Prasad[64,50], H. Qi[64,50], H. R. Qi[53], M. Qi[35], T. Y. Qi[9,g], S. Qian[1,50], W. B. Qian[55], Z. Qian[51],
C. F. Qiao[55], J. J. Qin[65], L. Q. Qin[12], X. P. Qin[9,g], X. S. Qin[42], Z. H. Qin[1,50], J. F. Qiu[1],
S. Q. Qu[36], S. Q. Qu[53], K. H. Rashid[66], K. Ravindran[21], C. F. Redmer[28], K. J. Ren[32],
A. Rivetti[67C], V. Rodin[56], M. Rolo[67C], G. Rong[1,55], Ch. Rosner[14], M. Rump[61], H. S. Sang[64],
A. Sarantsev[29,c], Y. Schelhaas[28], C. Schnier[4], K. Schoenning[68], M. Scodeggio[24A,24B],
K. Y. Shan[9,g], W. Shan[19], X. Y. Shan[64,50], J. F. Shangguan[47], L. G. Shao[1,55], M. Shao[64,50],
C. P. Shen[9,g], H. F. Shen[1,55], X. Y. Shen[1,55], B.-A. Shi[55], H. C. Shi[64,50], R. S. Shi[1,55], X. Shi[1,50],
X. D Shi[64,50], J. J. Song[15], W. M. Song[27,1], Y. X. Song[39,h], S. Sosio[67A,67C], S. Spataro[67A,67C],
F. Stieler[28], K. X. Su[69], P. P. Su[47], Y.-J. Su[55], G. X. Sun[1], H. K. Sun[1], J. F. Sun[15], L. Sun[69],
S. S. Sun[1,55], T. Sun[1,55], W. Y. Sun[27], X Sun[20,i], Y. J. Sun[64,50], Y. Z. Sun[1], Z. T. Sun[42],
Y. H. Tan[69], Y. X. Tan[64,50], C. J. Tang[46], G. Y. Tang[1], J. Tang[51], L. Y Tao[65], Q. T. Tao[20,i],
J. X. Teng[64,50], V. Thoren[68], W. H. Tian[44], Y. T. Tian[25], I. Uman[54B], B. Wang[1], D. Y. Wang[39,h],
F. Wang[65], H. J. Wang[31,k,l], H. P. Wang[1,55], K. Wang[1,50], L. L. Wang[1], M. Wang[42],
M. Z. Wang[39,h], Meng Wang[1,55], S. Wang[9,g], T. J. Wang[36], W. Wang[51], W. H. Wang[69],
W. P. Wang[64,50], X. Wang[39,h], X. F. Wang[31,k,l], X. L. Wang[9,g], Y. D. Wang[38], Y. F. Wang[1,50,55],
Y. Q. Wang[1], Y. Y. Wang[31,k,l], Ying Wang[51], Z. Wang[1,50], Z. Y. Wang[1], Ziyi Wang[55],
Zongyuan Wang[1,55], D. H. Wei[12], F. Weidner[61], S. P. Wen[1], D. J. White[59], U. Wiedner[4],
G. Wilkinson[62], M. Wolke[68], L. Wollenberg[4], J. F. Wu[1,55], L. H. Wu[1], L. J. Wu[1,55], X. Wu[9,g],
X. H. Wu[27], Y. Wu[64], Z. Wu[1,50], L. Xia[64,50], T. Xiang[39,h], H. Xiao[9,g], S. Y. Xiao[1], Y. L. Xiao[9,g],
Z. J. Xiao[34], X. H. Xie[39,h], Y. G. Xie[1,50], Y. H. Xie[6], Z. P. Xie[64,50], T. Y. Xing[1,55], C. F. Xu[1],
C. J. Xu[51], G. F. Xu[1], Q. J. Xu[13], S. Y. Xu[63], W. Xu[1,55], X. P. Xu[47], Y. C. Xu[55], F. Yan[9,g],
L. Yan[9,g], W. B. Yan[64,50], W. C. Yan[73], H. J. Yang[43,f], H. X. Yang[1], L. Yang[44], S. L. Yang[55],
Y. X. Yang[1,55], Yifan Yang[1,55], Zhi Yang[25], M. Ye[1,50], M. H. Ye[7], J. H. Yin[1], Z. Y. You[51],
B. X. Yu[1,50,55], C. X. Yu[36], G. Yu[1,55], J. S. Yu[20,i], T. Yu[65], C. Z. Yuan[1,55], L. Yuan[2],
S. C. Yuan[1], X. Q. Yuan[1], Y. Yuan[1], Z. Y. Yuan[51], C. X. Yue[32], A. A. Zafar[66], X. Zeng[6],
Y. Zeng[20,i], Y. H. Zhan[51], A. Q. Zhang[1], B. L. Zhang[1], B. X. Zhang[1], G. Y. Zhang[15], H. Zhang[64],
H. H. Zhang[27], H. H. Zhang[51], H. Y. Zhang[1,50], J. L. Zhang[70], J. Q. Zhang[34], J. W. Zhang[1,50,55],
J. Y. Zhang[1], J. Z. Zhang[1,55], Jianyu Zhang[1,55], Jiawei Zhang[1,55], L. M. Zhang[53], L. Q. Zhang[51],
Lei Zhang[35], P. Zhang[1], Shulei Zhang[20,i], X. D. Zhang[38], X. M. Zhang[1], X. Y. Zhang[42],
X. Y. Zhang[47], Y. Zhang[62], Y. T. Zhang[73], Y. H. Zhang[1,50], Yan Zhang[64,50], Yao Zhang[1],
Z. H. Zhang[1], Z. Y. Zhang[36], Z. Y. Zhang[69], G. Zhao[1], J. Zhao[32], J. Y. Zhao[1,55], J. Z. Zhao[1,50],
Lei Zhao[64,50], Ling Zhao[1], M. G. Zhao[36], Q. Zhao[1], S. J. Zhao[73], Y. B. Zhao[1,50], Y. X. Zhao[25],
Z. G. Zhao[64,50], A. Zhemchugov[29,a], B. Zheng[65], J. P. Zheng[1,50], Y. H. Zheng[55], B. Zhong[34],
C. Zhong[65], X. Zhong[51], L. P. Zhou[1,55], Q. Zhou[1,55], X. Zhou[69], X. K. Zhou[55], X. R. Zhou[64,50],
X. Y. Zhou[32], Y. Z. Zhou[9,g], A. N. Zhu[1,55], J. Zhu[36], K. Zhu[1], K. J. Zhu[1,50,55], S. H. Zhu[63],
T. J. Zhu[70], W. J. Zhu[9,g], W. J. Zhu[36], Y. C. Zhu[64,50], Z. A. Zhu[1,55], B. S. Zou[1], J. H. Zou[1]

1   *Institute of High Energy Physics, Beijing 100049, People's Republic of China*
2   *Beihang University, Beijing 100191, People's Republic of China*
3   *Beijing Institute of Petrochemical Technology, Beijing 102617, People's Republic of China*
4   *Bochum Ruhr-University, D-44780 Bochum, Germany*
5   *Carnegie Mellon University, Pittsburgh, Pennsylvania 15213, U.S.A.*
6   *Central China Normal University, Wuhan 430079, People's Republic of China*
7   *China Center of Advanced Science and Technology, Beijing 100190, People's Republic of China*
8   *COMSATS University Islamabad, Lahore Campus, Defence Road, Off Raiwind Road, 54000 Lahore,*
    Pakistan
9   *Fudan University, Shanghai 200433, People's Republic of China*
10 *G.I. Budker Institute of Nuclear Physics SB RAS (BINP), Novosibirsk 630090, Russia*
11 *GSI Helmholtzcentre for Heavy Ion Research GmbH, D-64291 Darmstadt, Germany*

12   *Guangxi Normal University, Guilin 541004, People's Republic of China*
13   *Hangzhou Normal University, Hangzhou 310036, People's Republic of China*
14   *Helmholtz Institute Mainz, Staudinger Weg 18, D-55099 Mainz, Germany*
15   *Henan Normal University, Xinxiang 453007, People's Republic of China*
16   *Henan University of Science and Technology, Luoyang 471003, People's Republic of China*
17   *Henan University of Technology, Zhengzhou 450001, People's Republic of China*
18   *Huangshan College, Huangshan 245000, People's Republic of China*
19   *Hunan Normal University, Changsha 410081, People's Republic of China*
20   *Hunan University, Changsha 410082, People's Republic of China*
21   *Indian Institute of Technology Madras, Chennai 600036, India*
22   *Indiana University, Bloomington, Indiana 47405, U.S.A.*
23   *INFN Laboratori Nazionali di Frascati, (A)INFN Laboratori Nazionali di Frascati, I-00044, Frascati, Italy; (B)INFN Sezione di Perugia, I-06100, Perugia, Italy; (C)University of Perugia, I-06100, Perugia, Italy*
24   *INFN Sezione di Ferrara, (A)INFN Sezione di Ferrara, I-44122, Ferrara, Italy; (B)University of Ferrara, I-44122, Ferrara, Italy*
25   *Institute of Modern Physics, Lanzhou 730000, People's Republic of China*
26   *Institute of Physics and Technology, Peace Ave. 54B, Ulaanbaatar 13330, Mongolia*
27   *Jilin University, Changchun 130012, People's Republic of China*
28   *Johannes Gutenberg University of Mainz, Johann-Joachim-Becher-Weg 45, D-55099 Mainz, Germany*
29   *Joint Institute for Nuclear Research, 141980 Dubna, Moscow region, Russia*
30   *Justus-Liebig-Universitaet Giessen, II. Physikalisches Institut, Heinrich-Buff-Ring 16, D-35392 Giessen, Germany*
31   *Lanzhou University, Lanzhou 730000, People's Republic of China*
32   *Liaoning Normal University, Dalian 116029, People's Republic of China*
33   *Liaoning University, Shenyang 110036, People's Republic of China*
34   *Nanjing Normal University, Nanjing 210023, People's Republic of China*
35   *Nanjing University, Nanjing 210093, People's Republic of China*
36   *Nankai University, Tianjin 300071, People's Republic of China*
37   *National Centre for Nuclear Research, Warsaw 02-093, Poland*
38   *North China Electric Power University, Beijing 102206, People's Republic of China*
39   *Peking University, Beijing 100871, People's Republic of China*
40   *Qufu Normal University, Qufu 273165, People's Republic of China*
41   *Shandong Normal University, Jinan 250014, People's Republic of China*
42   *Shandong University, Jinan 250100, People's Republic of China*
43   *Shanghai Jiao Tong University, Shanghai 200240, People's Republic of China*
44   *Shanxi Normal University, Linfen 041004, People's Republic of China*
45   *Shanxi University, Taiyuan 030006, People's Republic of China*
46   *Sichuan University, Chengdu 610064, People's Republic of China*
47   *Soochow University, Suzhou 215006, People's Republic of China*
48   *South China Normal University, Guangzhou 510006, People's Republic of China*
49   *Southeast University, Nanjing 211100, People's Republic of China*
50   *State Key Laboratory of Particle Detection and Electronics, Beijing 100049, Hefei 230026, People's Republic of China*
51   *Sun Yat-Sen University, Guangzhou 510275, People's Republic of China*
52   *Suranaree University of Technology, University Avenue 111, Nakhon Ratchasima 30000, Thailand*
53   *Tsinghua University, Beijing 100084, People's Republic of China*
54   *Turkish Accelerator Center Particle Factory Group, (A)Istinye University, 34010, Istanbul, Turkey; (B)Near East University, Nicosia, North Cyprus, Mersin 10, Turkey*
55   *University of Chinese Academy of Sciences, Beijing 100049, People's Republic of China*
56   *University of Groningen, NL-9747 AA Groningen, The Netherlands*

[57] University of Hawaii, Honolulu, Hawaii 96822, U.S.A.

[58] University of Jinan, Jinan 250022, People's Republic of China

[59] University of Manchester, Oxford Road, Manchester, M13 9PL, United Kingdom

[60] University of Minnesota, Minneapolis, Minnesota 55455, U.S.A.

[61] University of Muenster, Wilhelm-Klemm-Str. 9, 48149 Muenster, Germany

[62] University of Oxford, Keble Rd, Oxford, U.K. OX13RH

[63] University of Science and Technology Liaoning, Anshan 114051, People's Republic of China

[64] University of Science and Technology of China, Hefei 230026, People's Republic of China

[65] University of South China, Hengyang 421001, People's Republic of China

[66] University of the Punjab, Lahore-54590, Pakistan

[67] University of Turin and INFN, (A)University of Turin, I-10125, Turin, Italy; (B)University of Eastern Piedmont, I-15121, Alessandria, Italy; (C)INFN, I-10125, Turin, Italy

[68] Uppsala University, Box 516, SE-75120 Uppsala, Sweden

[69] Wuhan University, Wuhan 430072, People's Republic of China

[70] Xinyang Normal University, Xinyang 464000, People's Republic of China

[71] Yunnan University, Kunming 650500, People's Republic of China

[72] Zhejiang University, Hangzhou 310027, People's Republic of China

[73] Zhengzhou University, Zhengzhou 450001, People's Republic of China

[a] Also at the Moscow Institute of Physics and Technology, Moscow 141700, Russia

[b] Also at the Novosibirsk State University, Novosibirsk, 630090, Russia

[c] Also at the NRC "Kurchatov Institute", PNPI, 188300, Gatchina, Russia

[d] Currently at Istanbul Arel University, 34295 Istanbul, Turkey

[e] Also at Goethe University Frankfurt, 60323 Frankfurt am Main, Germany

[f] Also at Key Laboratory for Particle Physics, Astrophysics and Cosmology, Ministry of Education; Shanghai Key Laboratory for Particle Physics and Cosmology; Institute of Nuclear and Particle Physics, Shanghai 200240, People's Republic of China

[g] Also at Key Laboratory of Nuclear Physics and Ion-beam Application (MOE) and Institute of Modern Physics, Fudan University, Shanghai 200443, People's Republic of China

[h] Also at State Key Laboratory of Nuclear Physics and Technology, Peking University, Beijing 100871, People's Republic of China

[i] Also at School of Physics and Electronics, Hunan University, Changsha 410082, China

[j] Also at Guangdong Provincial Key Laboratory of Nuclear Science, Institute of Quantum Matter, South China Normal University, Guangzhou 510006, China

[k] Also at Frontiers Science Center for Rare Isotopes, Lanzhou University, Lanzhou 730000, People's Republic of China

[l] Also at Lanzhou Center for Theoretical Physics, Lanzhou University, Lanzhou 730000, People's Republic of China

[m] Also at the Department of Mathematical Sciences, IBA, Karachi, Pakistan